HHS Public Access

Author manuscript

Immunity. Author manuscript; available in PMC 2024 April 11.

Published in final edited form as:

Immunity. 2023 April 11; 56(4): 829–846.e8. doi:10.1016/j.immuni.2023.01.033.

The gut microbiota promotes distal tissue regeneration via RORγ⁺ regulatory T cell emissaries

Bola S. Hanna[1,2], **Gang Wang**[1,2], **Silvia Galván-Peña**[1,2], **Alexander O. Mann**[1,2], **Ricardo N. Ramirez**[1,2], **Andrés R. Muñoz-Rojas**[1,2], **Kathleen Smith**[3], **Min Wan**[3], **Christophe Benoist**[1,2], **Diane Mathis**[1,2,4,*]

[1]Department of Immunology, Harvard Medical School

[2]Evergrande Center for Immunologic Diseases, Harvard Medical School and Brigham and Women's Hospital, Boston MA 02115, USA

[3]Internal Medicine Research Unit, Worldwide Research, Development & Medical, Pfizer Inc., Cambridge, Massachusetts, USA.

[4]Lead Contact

SUMMARY

Specific microbial signals induce the differentiation of a distinct pool of RORγ⁺ regulatory T (Treg) cells crucial for intestinal homeostasis. We discovered highly analogous populations of microbiota-dependent Treg cells that promote tissue regeneration at extra-gut sites, notably acutely injured skeletal muscle and fatty liver. Inflammatory meditators elicited by tissue damage combined with MHC-class-II-dependent T cell activation to drive the accumulation of gut-derived RORγ⁺ Treg cells in injured muscle, wherein they regulated the dynamics and tenor of early inflammation and helped balance the proliferation versus differentiation of local stem cells. Reining in IL-17A-producing T cells was a major mechanism underlying the rheostatic functions of RORγ⁺ Treg cells in compromised tissues. Our findings highlight the importance of gut-trained Treg cell emissaries in controlling the response to sterile injury of non-mucosal tissues.

eTOC BLURB

Colonic RORγ⁺ Treg cells are a specialized microbiota-dependent population crucial for intestinal homeostasis, but their role in extra-gut tissues remains unexplored. *Hanna et al.* report that

[*]**Address correspondence to:** Diane Mathis, Department of Immunology, Harvard Medical School, 77 Avenue Louis Pasteur, Boston, MA 02115, dm@hms.harvard.edu, Phone: (617) 432-7741.

AUTHOR CONTRIBUTIONS

B.S.H., G.W., S.G.P., A.O.M., and K.S. performed experiments. B.S.H., R.N.R., A.R.M analyzed and interpreted data. B.S.H. and D.M. designed the study and wrote the manuscript, which all authors reviewed. M.W., C.B., and D.M. provided supervision. D.M. furnished funding.

COMPETING INTERESTS

D.M. is a co-founder and member of the Scientific Advisory Board of Abata Therapeutics.

these cells seed non-mucosal tissues in response to injury wherein they can rein in IL-17-driven inflammation, regulate stem cell activities and promote tissue regeneration.

Graphical Abstract

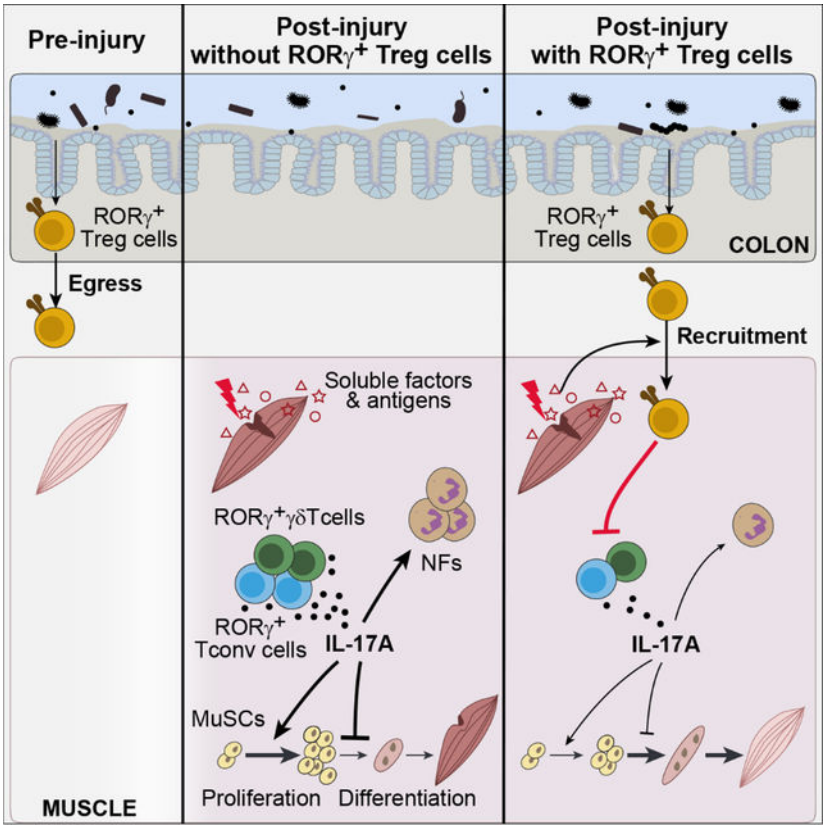

Keywords

Muscle; Colon; Microbiota; Treg; RORγ; IL-17; Tissue regeneration; Stem cell

INTRODUCTION

Foxp3-expressing Treg cells are a subset of $CD4^+$ T lymphocytes key for maintaining immunological tolerance. So-called “tissue-Treg cells” are a specialized category of Treg cells, with distinct transcriptomes and T cell receptor (TCR) repertoires, that are located in nonlymphoid tissues – for example, visceral adipose tissue, skeletal muscle, skin, and the colonic lamina propria[1]. Powered by their ability to dynamically cross-talk with a wide array of immunological and non-immunological cells in their microenvironment, tissue-Treg cells exert diverse functions, and thereby guard tissue homeostasis in various contexts, such as regulating local and systemic metabolism, enforcing tolerance to the microbiota, and regulating tissue regeneration in response to injury[1–10]. This diverse functional palette can manifest even within the same organ, as highlighted by skeletal muscle[7,11]. Treg cells rapidly accumulate in response to sterile muscle injury and promote tissue regeneration via

two major modes: 1) by controlling the activities of innate and adaptive immunocytes; and 2) by enhancing the regenerative capacity of muscle satellite cells (MuSCs), at least in part through secretion of the growth factor Areg.

While surveying Treg cell heterogeneity in nonlymphoid tissues, we noticed a population of RORγ$^+$ Treg cells that accrued in regenerating skeletal muscle early after acute injury. Unlike the majority of Treg cells generated as such in the thymus, intestinal RORγ$^+$ Treg cells are mostly locally induced in response to microbial or food antigens[3–5,12,13]. The function of RORγ$^+$ Treg cells has so far been linked primarily to mucosal health as they play an indispensable role in maintaining intestinal tolerance, with their loss resulting in increased incidences of colitis, colon cancer and food allergies[3,4,12,14–16].

In addition to its role in shaping the gut immune system, impacts of the microbiota on systemic immunity are increasingly evident. So far, such effects are best characterized for the effector arm of the adaptive immune system, where multiple effector T (Teff) cell subtypes generated or educated in the gut in response to microbial signals influence immunity at distal sites[17–24]. In contrast, whether RORγ$^+$ Treg cells play a role beyond their local function in mucosal tissues remains essentially unexplored. Our observation of a population of RORγ$^+$ Treg cells in regenerating skeletal muscle prompted us to investigate whether intestinal RORγ$^+$ Treg cells can drive tissue homeostasis at distal sites, thereby constituting a mode of cross-tissue communication coordinated by microbiota:Treg cell interactions.

RESULTS

scRNA-seq identifies a population of RORγ$^+$ Treg cells that accumulate in skeletal muscle at early times after acute injury

In response to the local damage provoked by intramuscular (i.m.) injection of cardiotoxin (CTX), Treg cells rapidly accumulate in regenerating muscle, peaking numerically at day 3–4 post-injury[7]. This timepoint marks transition of the tissue milieu from a pro- to an anti-inflammatory state, a step that is critical for efficient repair[7,25]. Considering the diverse cellular interactions in which muscle Treg cells participate in this complex, dynamic microenvironment[7,11,26,27], we investigated their transcriptional heterogeneity three days after CTX-induced injury via single-cell RNA sequencing (scRNA-seq) [quality-control metrics in Table S1]. Clustering, visualized by Uniform Manifold Approximation and Projection (UMAP), revealed five distinct groupings (Figure 1A). According to the transcripts differentially expressed by these clusters, we identified them as “resting”, “early-activation”, “reparative”, “RORγ$^+$”, and “interferon (IFN)-responding” Treg cells (Figure S1A–F). Most relevant here, expression of *Rorc*, encoding the RORγ transcription factor (TF), distinguished the RORγ$^+$ cluster, which also preferentially expressed colonic RORγ$^+$ Treg cell marker genes such as *Maf* (encoding c-Maf), and *Rorc* target loci such as *Ltb4r1* and *Furin* (Figures 1B, S1A, E).

Our attention was quickly drawn to the largely non-overlapping expression patterns of *Rorc* and *Ikzf2*, which encodes Helios (Figure 1B). *Ikzf2* showed an expression gradient spanning the reparative and part of the early-activation clusters, while expression of *Rorc*

was elsewhere and more circumspect. Since an essentially non-overlapping expression pattern of RORγ and Helios is characteristic of the intestinal Treg compartment[3,4], we further addressed the identity of the seemingly analogous muscle Treg cell clusters by superimposing the transcriptional signatures distinguishing colonic RORγ$^+$ and Helios$^+$ Treg cells on the UMAP (STAR Methods for details). As observed for the driving TFs, expression of the two signatures was essentially bimodal: the colonic RORγ$^+$ Treg cell up-signature was enriched in the muscle RORγ$^+$ cluster whereas the colonic Helios$^+$ up-signature was highest in the reparative and early-activation clusters (Figure 1C).

In search of clues to their function in muscle regeneration, we examined the transcriptome of muscle RORγ$^+$ Treg cells *vis-à-vis* other local subtypes (Figure S1G). Several of the up-regulated transcripts in muscle RORγ$^+$ Treg cells encoded proteins that promote immunocyte recruitment to inflammatory sites (e.g. *Ccr2*, *Ccr4, Cxcr6*, *Ltb4r1*) as well as cytoskeleton and cell adhesion proteins (e.g. *Vim*, *Actg1*, *Rac2* and *Cdc42*). Additionally, this cluster preferentially made more transcripts encoding a distinct set of Treg cell effector molecules (e.g. *Gzmb*, *Lgals1*, *Lgals3 and Furin*) and proteins known to dampen the function of inflammatory cells (e.g. *Il1r2*, *Anxa1*, *Cd47, Serpinb1a* and *Slamf6*). Pathway analysis of genes preferentially up-regulated in the muscle RORγ$^+$ cluster highlighted cell locomotion and extravasation pathways (Figure S1H).

We then examined the expression of RORγ and Helios in Treg cells from skeletal muscle as well as other relevant tissues at the protein level using flow cytometry (Figure 1D). As expected, colonic Treg cells included a much larger fraction of RORγ$^+$Helios$^-$ Treg cells (referred to as RORγ$^+$ Treg cells from here on) than did Treg cells from the spleen and muscle-draining inguinal lymph nodes (iLNs), of which RORγ$^-$Helios$^+$ Treg cells (referred to as Helios$^+$ Treg cells from here on) were the predominant population. Uninjured muscle harbored a small population of RORγ$^+$ Treg cells comprising 0–10% of the Treg compartment at steady-state. Three days after CTX-induced injury, a sizable population of RORγ$^+$ Treg cells had accumulated in regenerating muscle, an increase not observed in other tissues.

Preferential expression of key RORγ$^+$ Treg cell marker genes was also confirmed at the protein level: c-Maf and CXCR6, markers of RORγ$^+$ Treg cells, were expressed in more muscle RORγ$^+$ than Helios$^+$ Treg cells (Figure S1I). Gata3 and ST2, markers of colonic Helios$^+$ Treg cells, showed the opposite pattern of expression. RORγ$^+$ Treg cells rapidly accumulated upon muscle injury, peaking at day 3 and declining thereafter, when Helios$^+$ Treg cells became the major population (Figure 1E).

These data revealed an unanticipated heterogeneity of Treg cells in regenerating skeletal muscle. They also uncovered a distinct “early-responder” population of RORγ$^+$ Treg cells rapidly accruing after acute skeletal muscle injury.

Muscle RORγ$^+$ Treg cells have a colonic provenance

To address the possibility that muscle RORγ$^+$ Treg cells arose either from Foxp3$^-$ CD4$^+$ conventional T (Tconv) cells that transdifferentiated locally upon recruitment or from lymphoid-organ Treg cells that acquired RORγ expression in regenerating muscle, we

transferred congenically marked, naïve, splenic Tconv (CD45.2$^+$) and Treg (CD45.1$^+$) cells into Treg-cell-depleted *Foxp3^{DTR}* mice (CD45.1$^+$2$^+$), subsequently subjected to muscle injury (Figure S2A). The few donor-derived Foxp3$^+$ cells detected in injured muscle lacked RORγ expression, suggesting that these cells were unlikely to be the main source of muscle RORγ$^+$ Treg cells.

Thus, it seemed more plausible that muscle injury promoted the migration of colonic RORγ$^+$ Treg cells to skeletal muscle, a possibility that we interrogated using multiple approaches. As a prelude, we used our recently published scRNA-seq data[28] to perform a two-way comparison of the transcriptomes of muscle RORγ$^+$ versus total spleen Treg cells on day 4 post-injury with those of colon RORγ$^+$ versus total spleen Treg cells. There was an evident similarity between the transcriptional profiles of muscle and colon RORγ+ Treg cells (Figure 2A). In both cases, there was enrichment of the colon RORγ$^+$ Treg cell up-signature, although more strongly so for the colon samples, as indicated by the off-diagonal cloud of transcripts on the fold-change/fold-change (FC/FC) plot. Both muscle and colon RORγ$^+$ Treg cells exhibited enrichment of transcripts encoding Treg cell effector molecules (e.g. *Gzmb*, *S100a4* and *S100a6*) and specific chemokine receptors (e.g. *Ccr2, Ccr4 and Ccr5*) while being relatively depleted of transcripts encoding naïve Treg cell markers (e.g. *Ccr7* and *Sell*). However, some transcripts, such as *Ccr9* (encoding a gut homing receptor), *Lag3 and Il10* were preferentially enriched in the colon cells. Such transcriptional differences were confirmed via population-level RNA-seq of sorted muscle *vs* colon RORγ$^+$ Treg cells (Figure S2B–D).

Two strategies were employed to evaluate the ability of the colonic T cell compartment to engender muscle RORγ$^+$ Treg cells. First, we transferred CD4$^+$ T cells from the spleen versus colon into T-cell-deficient *Tcrb$^{-/-}$* mice, followed by acute muscle injury (Figure 2B). We chose to transfer total CD4$^+$ T cells rather than sorted Foxp3$^+$ cells in order to avoid the previously documented unphysiological outgrowth of cells with unstable Foxp3 expression when Treg cells are transferred alone into lymphopenic mice[29]. Three days post-injury, the RORγ$^+$ subtype constituted a much larger fraction of both the colon and muscle Treg compartments in mice transferred with colonic compared with splenic CD4$^+$ T cells (Figure 2B). Second, we turned to the Kaede transgenic mouse system, wherein the photoconvertible fluorescent reporter, Kaede, is ubiquitously expressed[30]. Upon exposure to violet light, reporter fluorescence irreversibly converts from green to red. By briefly photoconverting part of the descending colon of Kaede mice using endoscopic laser exposure, one can conveniently tag a fraction of colonic leukocytes and subsequently track their trafficking from the gut to extra-gut tissues (Figure 2C). Our previous studies using this system revealed active migration of most leukocyte classes from the colon to extra-gut lymphoid organs even at steady-state[31]. Forty-eight hours after photoconversion, colonic B cells, which generally display the most active emigration amongst colonic lymphocytes[31], migrated to skeletal muscle of both uninjured and injured mice (Figure 2D). Treg cells of colonic origin were not detectable in uninjured muscle, whereas CTX-induced injury consistently provoked their muscle accumulation (Figure 2D). The muscle RORγ$^+$ and Helios$^+$ Treg populations both contained cells of colonic origin, somewhat more in the RORγ$^+$ compartment (Figure 2E).

We also exploited TCR sequence information as a cellular barcode to examine the ontogenic relationship between muscle and colonic Treg cells, in particular between the RORγ$^+$ subtypes of these two organs. We performed scRNA-seq paired with sc*Tcr*-seq on matched muscle and colon Treg cells from six individual mice 3 days after CTX-induced injury. Clustering analysis of the muscle Treg cell scRNA-seq data largely recapitulated the major Treg cell subtypes we previously identified, the set of diagnostic transcripts of each cluster and, most importantly, the dichotomous expression pattern of *Rorc* and *Ikzf2* (Figures 2F, S2E–K). For colonic Treg cells, 6 distinct clusters emerged (Figure S2L). Of relevance to this study, we split them broadly into RORγ$^+$ and Helios$^+$ cells based on *Rorc* vs *Ikzf2* transcripts and their expression of the colon RORγ$^+$ vs Helios$^+$ Treg signatures (Figures 2G, S2N). Data integration confirmed a balanced distribution of cells from the two independent experiments across different clusters in both muscle and colon (Figure S2E, M).

We then used the TCR information to determine the degree of clonal expansion (≥2 cells sharing the exact same *Tcra* and *Tcrb* nucleotide sequences) in each subtype in each organ. In contrast to the polyclonal nature of most Treg cells in lymphoid organs[7], both muscle and colon Treg cell subtypes displayed a less diverse TCR repertoire, with expansion of multiple clones (Figure 2F, G). There was a considerable degree of intra-muscle and intra-colon clonotype sharing (Figures 2H, S2O). Notably, we detected multiple incidences of sharing between muscle and colon Treg cells, mostly between the two RORγ$^+$ subtypes (Figure 2H, I). A smaller fraction of muscle Treg cells, mostly restricted to the muscle reparative cluster, showed clonal overlap with the colonic Helios$^+$ Treg compartment. To further highlight the preferential clonal overlap between muscle and colon RORγ$^+$ Treg cells, we used the *scRepertoire* package[32] to calculate, for each individual mouse, an overlap score between all muscle Treg cell subtypes and colon RORγ$^+$ vs Helios$^+$ Treg cells. The score was highest between muscle and colon RORγ$^+$ Treg cells (Figure 2J).

In brief, multiple experimental approaches provided data arguing that muscle RORγ$^+$ Treg cells were engendered in the colon. Muscle and colon RORγ$^+$ Treg cells shared transcriptional particularities and TCR specificities. Both adoptive transfer and phototagging experiments evidenced colon to muscle cell flow.

RORγ$^+$ Treg cell accumulation in regenerating muscle depends on induction of soluble factors and TCR:MHC-II interactions

In search of mediators of RORγ$^+$ egress from the colon, we focused on sphingosine-1-phosphate receptors (S1PRs) since they are increasingly appreciated as regulators of lymphocyte egress from nonlymphoid tissues in addition to their classical role in regulating lymph node exit[33–36]. Kaede mice were treated with the drug FTY720, which provokes S1PR downregulation, followed by photoconversion of the distal colon. As expected[31], a fraction of Tconv cells, RORγ$^+$, and Helios$^+$ Treg cells had egressed from the colon of vehicle-treated mice by 24 hours, evidenced by a drop in the Kaede-red pool retained in the colon (Figure 3A). Concomitantly, colon-derived immigrants were readily detectable in the spleen (Figure 3B). FTY720 treatment completely abrogated both egress of these cells from the colon and their appearance in the spleen (Figure 3A, B), indicating that S1PRs strictly

regulated the egress of multiple types of $CD4^+$ lymphocytes from the colon to extra-gut tissues at steady-state.

FTY720 treatment of B6 mice resulted in a large drop in the numbers of muscle $ROR\gamma^+$ Treg cells at various timepoints post-injury (Figure 3C). Since FTY720 can impair lymphocyte egress from lymphoid organs, we turned back to the Kaede system to specifically address whether S1PRs were required for colon-derived $ROR\gamma^+$ Treg cell emigration to regenerating muscle. Using the experimental scheme illustrated in Figure 2C, we detected tagged colonic Tconv cells, $ROR\gamma^+$, and $Helios^+$ Treg cells in muscles of vehicle-treated mice 48 hours after injury. FTY720 almost completely abolished the migration of colonic $ROR\gamma^+$ Treg cells to regenerating muscle (Figure 3D). The drop in muscle $ROR\gamma^+$ Treg cell numbers in drug-treated mice was not due to increased cell death, either in the colon or in muscle, as indicated by comparable staining of cleaved caspase-3 (Figure S3A).

Several points argued against the possibility that muscle injury promoted $ROR\gamma^+$ Treg cell migration from the colon to injured muscle by more indirect or non-specific means. We did not observe any differences in the major immunocyte populations of the colonic lamina propria of control versus CTX-injured mice (Figures 1D, S3B). Nor did we detect a significant change in lymphocyte egress from the colon in injured compared with uninjured mice (Figure S3C). Consistently, CTX-induced injury did not result in increased intestinal permeability (Figure S3D), excluding the possibility that increased gut leakiness was the cause of muscle $ROR\gamma^+$ Treg cell accumulation.

As injury did not detectably influence colonic egress of $ROR\gamma^+$ Treg cells, we sought to identify inflammatory mediators whose receptors were expressed by $ROR\gamma^+$ Treg cells and whose expression was locally induced early after muscle injury. The scRNA-seq data introduced in Figure 1A revealed significant upregulation of transcripts encoding CCR2 and LTB4R1 (Leukotriene B4 receptor 1) in both colonic and muscle $ROR\gamma^+$ Treg cells (Figures 2A, S1E). Additionally, the ligands for both these receptors, CCL2 and LTB4, are well-established early inflammatory mediators, rapidly produced by invading myeloid cells and local stromal cells in response to injury[37,38]. We treated CTX-injured mice with a CCL2 neutralizing antibody or with an LTB4R1-specific antagonist, CP-105696. Administration of either agent reduced the representation of muscle $ROR\gamma^+$, but not $Helios^+$, Treg cells 2 days after CTX injection (Figures 3E, S3E), suggesting that CCL2 and LTB4 preferentially attracted $ROR\gamma^+$ Treg cells to injured muscle.

We also explored whether local signals promoted proliferation and/or retention of the recruited $ROR\gamma^+$ Treg cells. Since muscle $ROR\gamma^+$ Treg cells displayed a restricted repertoire of TCRs (Figure 2F–H), we focused on TCR:MHC-II interactions, a pivotal axis in controlling tissue-Treg cell accumulation in multiple contexts[1,39–41]. We performed short-term antibody-mediated MHC-II blockade in CTX-injured mice, and analyzed the muscle Treg compartment 3 days post-injury. MHC-II blockade induced an ~40% drop in muscle $ROR\gamma^+$ Treg cell numbers and a decrease in their fraction of cycling cells (Figure 3F, G). As expected, the numbers and cycling of $Helios^+$ muscle Treg cells were also affected by MHC-II blockade (Figure S3F, G). Reductions in $ROR\gamma^+$ Treg cell numbers and

proliferation after short-term MHC-II blockade were not observed in the spleen, mesenteric lymph nodes (mLNs), or colon (Figure S3H, I), in line with reports that antigen presentation by specialized cells in the mLNs is required for the induction of colonic RORγ$^+$ Treg cells early in life, but not for their maintenance in adulthood[42].

Considering the results from this multi-pronged analysis, we favor the following scenario: Under steady-state conditions, RORγ$^+$ (and other subtypes of) Treg cells generated in the colon constantly exit and redistribute through extra-gut lymphoid and non-lymphoid organs, being retained at sites where their TCR happens to recognize an antigen. Muscle injury induces the release of inflammatory stimuli such as CCL2 and LTB4, (perhaps coupled with increased antigen release), promoting recruitment of RORγ$^+$ Treg cells, where those with TCRs that recognize muscle antigen(s) preferentially proliferate and are retained.

Muscle RORγ$^+$ Treg cells are microbiota-dependent

One of the fundamental characteristics of intestinal RORγ$^+$ Treg cells is their dependence on the microbiota[3–5]. Since our investigations pointed to colonic RORγ$^+$ Treg cells as the original source of their muscle counterparts, we evaluated the microbiota dependence of muscle RORγ$^+$ Treg cells by comparing their representation in germ-free (GF) vs specific-pathogen-free (SPF) mice and in antibiotic (Abx)- vs vehicle-treated animals. GF mice showed minimal RORγ$^+$ Treg cell accumulation in muscle 3 days after CTX injection (Figures 4A, S4A). Similarly, treatment of SPF mice with a broad-spectrum Abx cocktail [ampicillin, neomycin, metronidazole and vancomycin; (VMNA)] drastically reduced the representation of muscle RORγ$^+$ Treg cells (Figures 4B, S4B). RORγ$^+$ Treg cell accumulation did not result from introduction of skin microbes during the injury process (Figure S4C, STAR Methods for details).

We performed scRNA-seq on sorted Treg cells 3 days after CTX-induced injury in mice treated with VMNA or vehicle (Figures 4C, S4 D–I). The distribution of cells across the UMAP space differed between vehicle- and VMNA-treated animals, with the latter being relatively depleted of the RORγ$^+$ cluster, while showing a proportional increase in the reparative and early-activation clusters (Figure 4C). Accordingly, muscle Treg cells from VMNA-treated animals had fewer transcripts preferentially expressed by RORγ$^+$ Treg cells, such as *Maf*, *Cxcr6* and *Ltb4r1*, while expressing more transcripts characteristic of reparative Treg cells, such as *Ikzf2*, *Gata3* and *Il1rl1* (Figure 4D), confirming the importance of microbial signals in shaping the muscle RORγ$^+$ Treg compartment.

These results raised the question of whether the impact of the microbiota on muscle RORγ$^+$ Treg cells was generic, or was specific to particular microbial strains. GF mice were monocolonized for 14 days with *C. ramosum*, which efficiently induces colonic RORγ$^+$ Treg cells, or with *P. magnus*, which does not[3], at which point hindlimb muscles were injected with CTX (Figure 4E). As expected, monocolonization with *C. ramosum,* but not *P. magnus*, restored colonic RORγ$^+$ Treg cells to SPF levels. Three days after CTX injection, *P. magnus*-monocolonized mice showed no increase in their muscle RORγ$^+$ Treg compartment above GF levels, whereas *C. ramosum*-monocolonized mice exhibited a specific expansion of the muscle RORγ$^+$ Treg population to a degree comparable with that of SPF mice (Figure 4F).

In sum, these data indicate that the specific microbial signals that induce RORγ$^+$ Treg cells in the colon predicate accumulation of the analogous RORγ$^+$ Treg population in regenerating muscle. And they provide additional confirmation of the colonic provenance of muscle RORγ$^+$ Treg cells.

Loss of muscle RORγ$^+$ Treg cells induces more local IL-17A-producing cells and impairs muscle regeneration

Abx treatment severely impairs muscle regeneration[43], probably due, at least in part, to the loss of microbiota-dependent RORγ$^+$ Treg cells (Figure 4A–F). But other lymphocyte populations, namely IL-17A-producing γδT cells, are similarly shaped by the microbiota and were recently reported to promote muscle regeneration[43]. So we addressed the functional relevance specifically of RORγ$^+$ Treg cells to muscle regeneration. Colonic RORγ$^+$ Treg cell differentiation is dependent on the TF c-Maf; hence *Foxp3*^{cre} × *Maf*$^{fl/fl}$ (*Maf*$^{\Delta Treg}$) mice, which harbor a deletion of *Maf* specifically in Treg cells, are impoverished in colonic RORγ$^+$ Treg cells[14,15]. Prior to injury, *Maf*$^{\Delta Treg}$ mice had a similar fraction of muscle Treg cells and a distribution of the major immunocyte compartments similar to those of their *Foxp3*^{cre} × *Maf*$^{wt/wt}$ (*Maf*^{wt}) littermate controls (Figures 5A, S5A). Three days after CTX injection, *Maf*$^{\Delta Treg}$ mice had a reduced fraction of muscle Treg cells (Figure 5A), with a diminished contribution of the RORγ$^+$ subtype (Figure 5B). In contrast, neither the fraction nor numbers of Helios$^+$ or Helios$^-$RORγ$^-$ Treg cell subsets were reduced (Figure S5B). In addition, ST2 and Areg, two key markers of reparative Helios$^+$ Treg cells, were similarly expressed in the two genotypes (Figure S5C). scRNA-seq of muscle Treg cells confirmed a reduced RORγ$^+$ cluster in *Maf*$^{\Delta Treg}$ mice, with proportional increases in the reparative and IFN-responding clusters (Figures 5C, S5E–J). Importantly, the reparative Treg cell cluster in *Maf*$^{\Delta Treg}$ mice showed typical expression of diagnostic signature genes (Figure S5D), further confirming that *Maf* deletion primarily impacted the muscle RORγ$^+$ Treg compartment, without obvious influences on other subtypes.

Having established the validity of *Maf*$^{\Delta Treg}$ mice as a model system, we probed the consequences of muscle RORγ$^+$ Treg cell loss by analyzing expression of T-bet, Gata3, and RORγ (key TFs for Th1, Th2, and Th17 cell differentiation, respectively) in the Tconv population of hindlimb muscles from *Maf*^{wt} and *Maf*$^{\Delta Treg}$ littermates. Three days after CTX injection, comparable fractions of T-bet$^+$ and Gata3$^+$ Tconv cells were observed in the two genotypes, whereas there was an increase in RORγ$^+$ Tconv cells in the mutant mice (Figures 5D, S5J). Accordingly, a higher percentage of Tconv cells from *Maf*$^{\Delta Treg}$ than from *Maf*^{wt} mice expressed IL-17A; but not IFNγ, IL-4, IL-5, or IL-13 (Figures 5E, S5K). In *Maf*$^{\Delta Treg}$ mice, muscle γδT cells, the main cell-type producing IL-17A after injury[43], had an increased proportion of IL-17A$^+$ cells (Figure 5E). These data demonstrate that muscle RORγ$^+$ Treg cells reined in a type-17 inflammatory response induced by muscle injury.

That RORγ$^+$ Treg cells also regulated muscle regeneration was established by comparing *Maf*^{wt} and *Maf*$^{\Delta Treg}$ mice 7 days post-injury via several assays. First, the mutant mice had more muscle neutrophils (NFs) (Figure 5F), a sign of poor resolution of inflammation. Secondly, histological analysis of individual muscle fibers revealed that mice lacking RORγ$^+$ Treg cells to have a significantly smaller distribution of fiber sizes and of the

average cross-sectional area than control littermates (Figure 5G), similar in magnitude to the difference previously reported for mice lacking reparative ($ST2^+$) Treg cells[26], and indicative of less efficient regeneration in the mutant mice. Thirdly, muscles from $Maf^{\Delta Treg}$ mice had greater collagen deposition, as measured by picrosirius red (PSR) staining (Figures S5L, 5H), signaling increased fibrosis, again a sign of poor muscle regeneration. Fourthly, as an orthogonal measure of tissue regeneration, we performed RNA-seq analysis on whole muscles from the two groups, and assessed expression of two gene modules previously demonstrated to dynamically change in response to injury: 1) an "inflammation + pre-repair" signature that is weakly expressed prior to injury, peaks at day 3–4, and is progressively turned off by days 7–14; and 2) a "homeostasis + structure" signature, comprised of genes involved in muscle filament structure and contractile function, which is turned down during active regeneration, and gradually turned back up by days 7–14[43]. $Maf^{\Delta Treg}$ mice aberrantly maintained up-regulation of the inflammation + pre-repair signature and down-regulation of the homeostasis + structure signature at day 7 post-injury (Figure 5I). These observations were confirmed with an independent set of inflammatory gene signatures characteristic of muscle injury[44] (Figure 5J).

In sum, muscle $ROR\gamma^+$ Treg cells are crucial for controlling local IL-17A production by multiple cell types. They also promote early resolution of inflammation and, ultimately, efficient tissue regeneration.

Failure to regulate IL-17A impairs MuSC differentiation and thereby muscle regeneration

Inflammatory cytokines such as tumor necrosis factor (TNF)α and IFNγ play key roles at early stages of muscle regeneration[11,25,45–49]. However, failure to down-regulate these same cytokines at subsequent stages is detrimental to the regenerative process, highlighting the need for dynamic regulation of inflammation. We recently reported that Tγδ17 and Th17 cells accumulate at early stages after muscle injury, which induces the proliferation of MuSCs and thereby promotes efficient regeneration[43]. Since depletion of $ROR\gamma^+$ Treg cells resulted in more cells making IL-17A (Figure 5E), failure to temporally regulate its production could paradoxically impede the process. Therefore, we compared the effects of administering rIL-17A early, late, or continuously after CTX-induced injury and evaluated muscle regeneration 7 days later (Figure 6A). These experiments were conducted on animals from Jackson Laboratory since they are known to have relatively low numbers of $ROR\gamma^+$ T cells and thus low basal IL-17A production[43], which enabled us to supplement IL-17A at diverse stages of tissue regeneration, and thereby simulate the impact of IL-17A dysregulation subsequent to the loss of $ROR\gamma^+$ Treg cells. Seven days after CTX injection, the cross-sectional area of individual muscle fibers in mice treated with rIL-17A at only early times after injury was increased compared with that of vehicle-treated controls (Figure 6B). In contrast, mice with late or continuous rIL-17A treatment did not exhibit a regenerative boost (Figure 6B). Additionally, late rIL-17A treatment resulted in more muscle NFs and greater muscle fibrosis (Figure 6C, D). These results illustrate the necessity of temporally correct regulation of IL-17A production during muscle regeneration: pro-reparative when restricted to early stages; anti-reparative with prolonged exposure.

To explore the mechanisms underlying the detrimental effects of prolonged IL-17A exposure, we first identified cells capable of expressing both chains of the IL-17R using previously published scRNA-seq data from injured muscle[50]. *Il17ra* transcripts were abundant in multiple immunologic and non-immunologic cell types, while transcripts of *Il17rc* were restricted to MuSCs and mesenchymal stromal cells (Figure S6A, B). Because of their obvious relevance, we focused on MuSCs, a population of quiescent stem cells that become activated and proliferate for a certain number of cycles in response to muscle injury[25,51,52]. They must then exit the cell cycle to initiate the highly orchestrated differentiation program leading to myocytes, which eventually fuse with each other and with existing myofibers to regenerate healthy muscle tissue. Consequently, various inflammatory cytokines that promote MuSC proliferation at early stages of injury can prohibit their myogenic differentiation upon prolonged exposure as they do not exit the cell cycle and myogenic TFs remain suppressed[48,49,53]. Thus, controlling inflammation could be an important checkpoint for effective muscle regeneration. RNA-seq of flow-cytometrically sorted MuSCs ($CD45^{-}CD31^{-}SCA\text{-}1^{-}VCAM\text{-}1^{+}$, Figure S6C) on days 0, 1, and 3 after injury revealed dynamic expression of *Il17ra* by MuSCs, highest at steady-state and progressively reduced on days 1 and 3 after injury (Figure 6E).

Next, we performed RNA-seq on sorted MuSCs from rIL-17A- or vehicle-treated mice on days 0, 1 and 3 after CTX-induced injury (administration scheme as per Figure 6A). k-means clustering of the MuSC time-course highlighted 15 gene clusters coordinately modulated during the regenerative process. Focusing on clusters differentially expressed between rIL-17A- and vehicle-treated mice at day 3 after injury, we identified a set of differentiation-related gene modules pertaining to muscle structure, myogenic differentiation and metabolism (TCA cycle and oxidative phosphorylation) with reduced expression in rIL-17A-treated mice (Figure 6F). Relatedly, expression of a previously identified myogenic differentiation signature[54] was down-regulated in MuSCs from rIL-17A-treated mice, as evidenced by the off-diagonal cloud on the FC/FC plot of Figure 6G. On the other hand, expression of a cell-division module was enriched in the rIL-17A-treated group (Figure 6F).

To determine whether this inhibitory effect reflected a direct impact of IL-17A on MuSCs, we sorted them from uninjured mice, and cultured them *in vitro* with or without rIL-17A under conditions that promote myogenic differentiation. In response to the isolation process and culturing with serum, MuSCs are activated and enter the cell cycle; subsequently, they commit to the myogenic fate and differentiate into myotubes[55]. After 2 days of culture, a greater fraction of rIL-17A-treated MuSCs were in cycle, as measured by EdU incorporation (Figure 6H). On day 3 and 4, we assessed MuSC differentiation by quantifying the expression of the myogenic commitment factor, Myogenin (MyoG), and myosin heavy chain (MyHC), a marker of differentiated myotubes. In line with the above-mentioned transcriptomic data (Figure 6 F, G), continuous rIl-17A treatment reduced the fraction of differentiated $MyoG^{+}$ and $MyHC^{+}$ cells (Figure 6I, J). These results agree with previous reports showing an inhibitory effect of IL-17A on MyoG expression and the consequent myogenic differentiation of myoblast cell lines[56].

Thus, our data indicate a direct, time-dependent impact of IL-17A on MuSCs, initially promoting their proliferation, but impeding their differentiation upon prolonged exposure.

Given the critical role of RORγ$^+$ Treg cells in the temporal regulation of IL-17A production in regenerating muscle (Figure 5E), timely recruitment of RORγ$^+$ Treg cells at early stages of regeneration appears to be crucial for shielding differentiating MuSCs from IL-17A, thereby promoting return to homeostasis.

RORγ$^+$ Treg cells regulate IL-17A-driven inflammation in a model of non-alcoholic steatohepatitis (NASH) in a microbiota-dependent manner

Lastly, we probed the generality of RORγ$^+$-Treg-cell-mediated inter-tissue communication. As a preliminary step, we examined RORγ expression in various tissue-Treg compartments at steady-state. A population of RORγ$^+$ Treg cells was detected in multiple extra-gut tissues, including the liver, lung and kidney, usually comprising 5–10% of the Treg pool (Figures 7A, S7A). As in the colon and muscle, the RORγ$^+$ Treg populations in these tissues were microbiota-dependent. Moreover, analysis of a previously published scRNA-seq dataset from CD4$^+$ T cells isolated from cardiac muscle after myocardial infarction[57] identified a distinct population of RORγ$^+$ Treg cells with a marker profile similar to that of their colonic and skeletal muscle counterparts (Figures 7B–C, S7B–F).

As the steady-state RORγ$^+$ Treg populations in liver, lung and kidney were generally smaller than that of regenerating muscle, we wondered whether they would increase in response to sterile injury or inflammation. We chose a diet-induced NASH model to address this question because the gut:liver axis has been implicated in promoting multiple hepatic pathologies, and because IL-17A-mediated inflammation plays a central role in NASH progression[58–60]. Feeding mice a choline-deficient, amino-acid-defined, high-fat diet (CDAHFD) rapidly induces hepatocellular death and inflammation, with mice succumbing to tissue fibrosis at later disease stages[61]. We analyzed liver RORγ$^+$ Treg cells after one week of CDAHFD feeding, an early time-point at which intestinal permeability and the colonic RORγ$^+$ Treg compartment were not altered, and observed a fractional and numerical increase in liver RORγ$^+$ Treg cells *vis-a-vis* mice fed control diet (Figures 7D, S7G–I). Mirroring our observations on regenerating skeletal muscle, the CDAHFD-induced increase in liver RORγ$^+$ Treg cells was abolished in VMNA-treated animals (Figure 7D).

To assess the functional relevance of RORγ$^+$ Treg cells in this context, we again turned to $Maf^{\Delta Treg}$ mice. At steady-state, mutant mice had a normal representation of the major immunocyte populations (Figure S7J). But, one week after the introduction of CDAHFD, they showed an increase in total liver Treg cells (Figure 7E), though a substantially reduced population of RORγ$^+$ Treg cells (Figure 7F). This reduction was accompanied by higher percentages of liver RORγ$^+$ Tconv and γδT cells (Figure 7G). Accordingly, the fraction of cells producing IL-17A, but not those making IFNγ, IL-4, IL-5 or IL-13, in $Maf^{\Delta Treg}$ mice was higher for both liver Tconv and γδT cells (Figures 7H, S7K, L).

IL-17A is a well-established driver of NASH pathology through its promotion of inflammation, metabolic dysregulation, and the fibrogenic machinery in hepatic stellate cells[59,60,62]. To explore impacts on these processes, we examined the effect of RORγ$^+$ Treg cell loss on whole-liver gene expression profiles after a brief course of CDAHFD feeding. 387 and 204 genes were significantly up- or down-regulated, respectively, >1.5-fold in $Maf^{\Delta Treg}$ compared with Maf^{wt} mice (Figure 7I). Loci preferentially expressed in the

mutant livers included metabolic genes implicated in NASH pathology (e.g *Pparg* and *Fabp4*), inflammatory genes (e.g. *Ccl5, Cx3cr1* and *Cd63*) and multiple extracellular matrix genes (e.g. *Col1a1*, *Col3a1*, *Col4a1* and *Timp3*). Consistently, pathway analysis pointed to epithelial-mesenchymal transition and immune-response modules as the top up-regulated pathways in the absence of RORγ$^+$ Treg cells (Figure 7J).

We questioned whether the early changes in response to injury would translate into increased NASH-induced fibrosis at later stages by analyzing *Maf*$^{\Delta Treg}$ mice after 8 weeks of CDAHFD feeding, a timepoint at which liver fibrosis has been established[61]. At this timepoint, the mutant mice showed a decreased fraction of RORγ$^+$, but not Helios$^+$, ST2$^+$, or Areg$^+$ Treg cells, as well as increased RORγ$^+$ and IL-17A$^+$ Tconv populations (Figure S7M–Q). In addition, they had an increased representation of inflammatory macrophages and NFs (Figure S7R). While the plasma concentrations of liver transaminases were comparable between the two genotypes (Figure S7S), *Maf*$^{\Delta Treg}$ livers had significantly larger fibrotic scars, as measured by PSR staining (Figure 7K), indicating a protective role of RORγ$^+$ Treg cells in inflammation-induced liver fibrosis.

These results serve to generalize our findings from regenerating muscle. The homeostatic function of microbiota-dependent RORγ$^+$ Treg cells extends far beyond the intestine to multiple non-mucosal tissues.

DISCUSSION

Our temporal scRNA-seq studies uncovered a population of RORγ$^+$ Treg cells accruing at early times after acute skeletal muscle injury. Explorations of these cells' role in muscle regeneration yielded several important insights: 1) that the microbiota regulated muscle repair via RORγ$^+$ Treg cells emanating from the gut; 2) that local inflammatory signals and TCR engagement drove their migration to and expansion within regenerating muscle; 3) that these Treg cells controlled the tenor and dynamics of injury-induced inflammation while also helping to balance the proliferative and differentiative activities of muscle stem cells; and 4) that RORγ$^+$ Treg cell emissaries from the gut appeared to play a general role in the homeostasis of extra-gut tissues.

The original discovery of RORγ$^+$ Treg cells as a microbiota-dependent subtype of colonic regulatory T cells emphasized their role as guardians of intestinal health through promotion of tolerance to food antigens and local microbes[3,4,12,14–16]. Here we demonstrated that the impact of colonic RORγ$^+$ Treg cells extended far beyond their site of generation: they formed a specialized pool of gut-trained regulators that could be rapidly mobilized in response to tissue emergencies at non-mucosal sites. Equipped with a distinct set of TCRs, homing receptors, and effector molecules, these cells orchestrated effective tissue regeneration and return to homeostasis. Since RORγ$^+$ Treg cells are thought to mainly react to commensal or food antigens, the TCR-mediated proliferation and retention of these cells in regenerating muscle raises the question of how local antigens promote this response. Cross-reactivity between microbial (including commensal) antigens and autoantigens is well-documented[63–69]. Thus, some form of epitope mimicry between microbial or food and muscle antigens might be at root, especially since that tissue damage and the associated

inflammation could increase the strength and breadth of autoantigen presentation. It is by now well established that enteric microbes can drive effector T cell responses to a variety of challenges outside the gut[17–21]. Extending this concept to Treg cells raises the possibility of a self-contained system of gut-trained effector and regulatory T cell recruits, which could both coordinate rapid and efficient return to homeostasis and avoid over-shooting of microbiota-induced inflammatory responses.

Tissue regeneration in general, and muscle regeneration in particular, is a dynamic, multi-cellular process in which temporal regulation of pro-inflammatory mediators is fundamental to fidelity and efficiency[25,45–49]. While crucial for the early response to tissue injury, pro-inflammatory molecules can paradoxically impede tissue repair if not controlled properly. We have uncovered a spike in various classes of IL-17A-producing cells early after muscle injury (herein and[43]); to our knowledge, IL-17A had not previously been associated with muscle repair. One function of IL-17A is to recruit NFs, which have important early roles in secreting mediators and clearing debris, but must be reined in at later times to permit effective tissue regeneration[43,70]. Akin to its role in expanding stem cell pools in other contexts[71–75], IL-17A also promoted the proliferation of MuSCs via two mechanisms: by directly stimulating their cell-cycle progression and, indirectly, by promoting the accumulation of NFs, which can also induce MuSC proliferation[70]. Our data highlight a rheostatic role for RORγ^+ Treg cells in controlling the dynamics of IL-17A activity along the course of tissue regeneration. By limiting the activity of IL-17A to early stages of injury, they shielded MuSCs from prolonged exposure to IL-17A, which could impair myocyte differentiation, resulting in inferior repair and enhanced fibrosis. Similar phenomena wherein IL-17A inhibits tissue stem-cell differentiation directly or indirectly (in the CNS and skin) have been observed[10,76].

Our data suggest that regulation of IL-17-mediated inflammation by microbiota-dependent RORγ^+ Treg cells may be a general axis in play across multiple extra-gut sites. Thus, dysbiotic gut conditions capable of inhibiting the generation or export of RORγ^+ Treg cells are likely to have systemic impacts on tissue homeostasis at multiple extra-gut sites. The potential for such detrimental outcomes advocates for judicious use of antibiotics after tissue injury. On the other hand, modulating RORγ^+ Treg cells via diet or personalized probiotics[77,78] could prove to be potent therapeutic add-ons in such contexts.

LIMITATIONS OF THE STUDY

Considering that a fraction of RORγ^+ Treg cells constantly egresses from the colon to extra-gut sites at steady state, it is not clear to what extent the RORγ^+ Treg population in injured muscle issued directly from the colon rather than first sojourning through one or more other tissues. Complex cell tracking experiments will be required to formally address this point. While injury-induced accumulation of RORγ^+ Treg cells depended on the ligands of CCR2 and LTB4R1, it is theoretically possible that this dependency reflects indirect effects on non-Treg cells expressing these receptors.

STAR★Methods

RESOURCE AVAILABILITY

Lead contact—Further information and requests for resources and reagents should be directed to and will be fulfilled by the lead contact, Diane Mathis (dm@hms.harvard.edu).

Materials availability—This study did not generate new unique reagents.

Data and code availability—Data newly reported in this paper were deposited in the Gene Expression Omnibus (GEO) database under accession no. GSE196338.

EXPERIMENTAL MODEL AND SUBJECT DETAILS

Mice—*Foxp3*$^{IRES\text{-}GFP}$ (*Foxp3*^{GFP}) mice[79] were obtained from V. Kuchroo (Brigham and Women's Hospital, Boston, MA). C57BL/6J, *Tcrb*$^{-/-}$ and B6.129P2(Cg)-*Rorc*$^{tm2Litt/J}$ (*Rorc*^{GFP}) mice[80] were purchased from Jackson Laboratory. The Kaede transgenic mouse line (B6.Kaede)[30], obtained from O. Kanagawa, and *Rorc*^{GFP} mice were crossed to *Foxp3*$^{Thy1.1}$ mice[81] (from A. Rudensky, Memorial Sloan Kettering Cancer Center, New York, NY). *Foxp3*^{DTR} mice[82] were obtained from A. Rudensky and crossed to B6.CD45.1 mice from Jackson Laboratory. To generate Treg-specific c-Maf-deficient mice, we crossed *Foxp3*^{Cre} mice[83] (from A. Rudensky) to *Maf*^{fl} mice[84] (from C. Birchmaier; Max Delbrück Center, Berlin, Germany). Six- to 12-wk-old male and female mice were used for all experiments. Sexes were not mixed in transcriptomic experiments. All mice were housed in our SPF facility at Harvard Medical School. All experiments were conducted under protocols approved by Harvard Medical School's Institutional Animal Care and Use Committee.

METHOD DETAILS

Mouse treatments and colonizations—To induce muscle injury, we anesthetized mice by intraperitoneal (i.p.) administration of ketamine:xylazine in combination (10 mg/kg: 2 mg/kg), and i.m.-injected them with 0.03 mL per muscle of CTX from *Naja mossambica* or *Naja pallida* (0.03 mg/mL; Sigma-Aldrich) in one or more hindlimb muscles (tibialis anterior (TA), gastrocnemius, quadriceps), as previously described[7]. To exclude the possibility that RORγ^+ Treg cell accumulation resulted from introduction of skin microbes during our standard injury protocol, we employed a sterile surgical procedure: the skin was opened and injury was induced without the needle passing through skin. As shown in Figure S4C, this approach yielded a fraction of RORγ^+ Treg cells similar to that induced by the standard injury protocol. To block egress of lymphocytes from peripheral organs, we i.p.-injected mice with 1 mg/kg of the S1P receptor agonist, FTY720 (Cayman Chemical), 4 hr prior to Kaede photoconversion or CTX-induced injury, and daily thereafter. For *in vivo* CCL2 and LTB4R1 blockade, mice were treated with anti-CCL2 neutralizing antibody (200 μg i.p.; clone 2H5) or with the LTB4R1 antagonist CP-105696 (20 mg/kg body weight by oral gavage; Sigma-Aldrich) 6 hr prior and 1 d after CTX injection. For *in vivo* MHC-II blockade, mice were i.p.-injected with 500 μg of anti-mouse I-A/I-E (clone M5/114) or rat IgG2b control (clone LTF-2) 6 hr prior to CTX-induced injury followed by 200 μg on each subsequent day. All *in vivo* antibodies were purchased from Bioxcell. For *in vivo* rIL-17A

administration, 500 ng of rIL-17A (Peprotech) was i.p.-injected in sterile phosphate buffered saline (PBS) at various timepoints pre- or post-injury, as indicated in the schematic diagram in Figure 6A. To increase muscle specificity, rIL-17A (100 ng/muscle) was i.m.-injected on day 0 along with CTX.

For mono-colonization, GF mice were orally gavaged with single bacterial species at 4 weeks of age for 2 weeks. Stool samples were collected and plated at 2 weeks to verify colonization and rule out contamination from other species. For Abx treatment, mice were treated with 0.5 mg/ml vancomycin (RPI), 1 mg/ml metronidazole (Sigma-Aldrich), 1 mg/ml neomycin (Fisher Scientific), 1 mg/ml ampicillin (Sigma-Aldrich) dissolved in drinking water for three weeks prior to muscle injury.

For liver studies, male mice were fed a control diet containing 10 kcal% Fat (A08051501i) or CDAHFD (A06071309i), both purchased from Research Diets.

Isolation of leukocytes from lymphoid and nonlymphoid tissues

Skeletal muscle: Isolation of skeletal muscle lymphocytes was done as previously described[7]. Briefly, hindlimb muscles were excised, minced and digested at 37°C for 30 min in a solution containing Dulbecco's Modified Eagle's Medium (DMEM, 2% fetal calf serum (FCS), collagenase II (2 mg/mL; Thermo Fisher Scientific) and DNase I (100 μg/mL; Sigma-Aldrich). Leukocytes were enriched by Percoll (GE Healthcare) density centrifugation (40%:80%, 25 min at 1,126 × g). The interphase containing leukocytes was recovered, washed, and stained for analysis or sorting by flow cytometry.

Colon: Intestinal tissues were cleaned and treated with Roswell Park Memorial Institute (RPMI) medium containing 1 mM dithiothreitol, 20 mM ethylenediaminetetraacetic acid (EDTA) and 2% FCS at 37°C for 15 min to remove epithelial cells, minced and dissociated in collagenase solution (1.5 mg/ml collagenase II (Gibco), 0.5 mg/ml dispase and 1% FCS in RPMI) with constant stirring at 37°C for 30 min. Single-cell suspensions were filtered and washed with 10% FCS RPMI solution before staining and sorting by flow cytometry.

Liver, lung and kidney: Mice were perfused with ice-cold PBS through the left ventricle of the heart. Tissues were excised and minced in DMEM containing collagenase IV (0.5 mg/ml; Gibco), DNase I (150 μg/ml; Sigma-Aldrich) and FCS (1%), and were incubated in a 37°C water bath with shaking for 30–45 min. Digested tissues were passed through a 70-μm cell strainer and washed in DMEM/FCS. Leukocytes from liver were enriched by Percoll density centrifugation (36%, 10 min at 800 × g) as previously described[85].

Spleen and lymph nodes: Lymphocytes were obtained by mechanical disruption, followed by red blood cell lysis, and filtered and washed with 10% RPMI solution.

Isolation and analysis of muscle stem cells—Isolation of muscle MuSCs was done as previously described[86]. Briefly, hindlimb muscles were minced and digested by collagenase II (800 U/ml) in Ham's F10 with 10% horse serum at 37°C for 90 min, followed by a second digestion step using collagenase II (80 U/ml) and dispase (11 U/ml) for 30 min.

Cell suspensions were passed through a 20-Gauge needle 10 times and then filtered through a 40-μm cell strainer, washed, and stained for analysis or sorting by flow cytometry.

Flow cytometry—The following antibodies were used for flow-cytometric staining: anti-CD4, -CD8a, -CD45, -CD45.1, -CD45.2, -Thy1.1, -CD44, -CXCR6, -CD11b, -CD3, -TCRγδ, -IL-17A, -IFN-γ, -IL-4, -IL-5, -CD31, -Sca-1, -VCAM-1, -Helios, -T-bet, all from Biolegend; and -Foxp3, -RORγt, -c-Maf, -Gata3, -ST2, -IL-13 from eBioscience; -TCRβ, -Ki-67 from BD; -Areg from R&D; and -cleaved caspase-3 from Cell Signaling. Surface staining was performed for 30 minutes at 4°C, and viability was assessed using Zombie UV™ Fixable Viability Dye (Biolegend) as per the manufacturer's instructions. Intracellular staining was performed using eBioscience™ Foxp3/Transcription Factor Staining Buffer Set. After surface staining of cells from Kaede mice, cells were fixed with 2% ice-cold paraformaldehyde for 30–60 min at 4°C, washed twice with PBS before proceeding to intracellular staining using eBioscience™ Foxp3/Transcription Factor Staining Buffer Set. For *ex vivo* intracellular cytokine and Areg staining, single-cell suspensions were stimulated for 3.5 hours at 37°C with 50 ng/mL phorbol 12-myristate 13-acetate (PMA) and 1 μM ionomycin (both from Sigma-Aldrich) in the presence of protein transport inhibitor cocktail (eBioscience) in complete RPMI-1640 media supplemented with 10% fetal bovine serum (Thermo Fisher Scientific). Cells were acquired with a FACSymphony flow cytometer (BD Biosciences). Data were analyzed using FlowJo software (Tree Star).

Cell transfers—Treg and Tconv cell transfers were performed as previously described[87]. Briefly, 10^5 Treg cells ($CD4^+TCR\beta^+Foxp3^{GFP+}$) or 10^6 naïve $CD4^+$ Tconv cells ($CD4^+TCR\beta^+CD44^{lo}Foxp3^{GFP-}$) were sorted from the spleens of CD45.1$^+$ *Foxp3^{GFP}* or B6.*Foxp3^{GFP}* mice, respectively using MoFlo (Beckman Coulter) and were i.v. injected into CD45.1$^+$/CD45.2$^+$ *Foxp3^{DTR}* hosts. At 1d prior and 1d after transfer, host Treg cells were depleted via i.p. injection with diphtheria toxin (Sigma-Aldrich) at 20 ng/g of body weight. For cell transfer into *Tcrb$^{-/-}$* mice, $CD4^+$ T cells were sorted from the spleen or colon of B6 mice, and matched cell numbers ($1–5 \times 10^5$ cells) were i.v. injected into recipient mice. All cell transfers were performed 2 weeks prior to CTX-induced injury.

Analysis of cell migration via the Kaede system—Kaede mice were anesthetized with ketamine:xylazine in combination (10 mg/kg:2 mg/kg i.p). Photoconversion of the descending colon was done as previously described[31]. A custom-built fiberoptic endoscope (ZIBRA Corporation) was coupled to the handheld 405-nm laser via an in-house, custom-made connection device (fixed mounts were purchased from ThorLabs). After cleansing the colon of fecal pellets with PBS, we inserted the fiberoptic endoscope through the anus into the descending colon to a depth of 2.5 cm. The laser was switched on, thereby exposing the inner colon to violet light (beam diameter was 3.5 mm). Subsequently, the endoscope was gently retracted, pausing at 2-mm increments for 30s light pulses at each interval (for a total of up to 10 min). The fractions of Kaede-red$^+$ cells in various immunocyte populations were analyzed by flow cytometry at the indicated time-points.

Single-cell studies—For standard genome-wide scRNA-seq analyses, Treg cells from hindlimb muscles of *Foxp3^{GFP}* or *Foxp3^{Cre}* × *Maf$^{fl/fl}$* mice were sorted by flow cytometry

and encapsulated using the Chromium Single Cell 3′ v3 platform. For coupled scRNA-seq and sc*Tcr*-seq, Treg or CD4$^+$ T cells from muscles and colon of six individual *Foxp3*^{GFP} mice were sorted and encapsulated using the Chromium Single Cell 5′ v1.1 and V(D)J platform (10x Genomics). In some experiments, individual samples were tagged (hashed) with DNA-coded anti-CD45/MHC-I antibodies (Biolegend). For standard scRNA-seq, data analysis was done as previously described[88,89]. Data were processed using the standard cellranger pipeline (10x Genomics). HTO counts were obtained using the CITE-seq-Count package. Single-cell data were analyzed using the Seurat package[90]. HTOs were assigned to cells using the HTODemux function, and doublets and negative cells were eliminated from analysis. Low quality cells and doublets were also excluded from the analysis according to the criteria in Table S1. Clusters encompassing Treg cells were determined based on the expression of Treg marker genes (e.g. *Foxp3, Il2ra, Ctla4 and Ikzf2*), while clusters encompassing non-Treg cells were removed from analysis using the SubsetData function. Data were normalized using the NormalizeData function and scaled using the ScaleData function. Variable genes were determined using the FindVariableGenes function. Principal components (PCs) were calculated using the RunPCA function, and top significant PCs were selected using JackStraw() and ElbowPlot() functions. Clustering was done on selected PCs using the FindNeighbors followed by the FindClusters functions, and UMAP dimensionality reduction was calculated using the RunUMAP function. Signature scoring was done with Seurat's AddModuleScore function. Differentially expressed genes were calculated using the FindAllmarkers and FindMarkers functions. Colon Treg signatures were generated from scRNAseq data of colonic CD4$^+$ T cells from SPF mice[88] using the FindMarkers function in Seurat to identify differentially expressed genes (>0.25 logFC with p-value<0.05) between RORγ^+ and Helios$^+$ colonic Treg cells. Visualization of expression density of transcripts or signature scores was done suing the Nebulosa package[91]. Comparison of colon and muscle RORγ^+ Treg transcriptomes was done using our previously published tissue-Treg scRNAseq dataset[28]. [Note: muscle Treg cells in this dataset were isolated at day 4 after injury. Since different batches of CTX induce muscle injury and repair with slightly different kinetics, the peak of inflammation can be on either day 3 or day 4. We routinely titer different batches of CTX to adjust the time course accordingly]. scRNA-seq of muscle, colon and matched total spleen Treg cells was analyzed using the standard Seurat pipeline, and the RORγ^+ Treg cluster in each tissue was identified by high expression of the colonic RORγ^+ Treg signature. Average expression of genes in each cluster was calculated using the AverageExpression function in Seurat, and FC/FC plots were generated by Multiplot Studio (GenePattern; Broad Institute) using matched spleen Treg samples as a comparator for RORγ^+ Treg cells in each tissue. Integration of scRNA-seq data from different experimental batches was done using the Harmony pipeline[92]. Analysis of previously published scRNA-seq dataset from cardiac muscle CD4$^+$ T cells after myocardial infarction[57] was done as described above. Briefly, clusters encompassing Treg cells were determined based on high expression of *Foxp3, Il2ra, Ctla4 and Ikzf2,* and clusters with high expression of Teff markers (e.g. *Ifng, Il17a, Il4*) were removed from analysis using the SubsetData function.

The *Tcr*-seq library was processed with the cellranger vdj pipeline (v4.0), using default parameters. This pipeline was used for the assignment of V and J genes, CDR3 regions and sequences. Resulting data were analyzed using the scRepertoire package[32]. Over two

independent experiments, we recovered 1529 and 3918 individual muscle and colon Treg cells, while retaining *Tcra* and *Tcrb* sequence information from 72 and 79% of the cells, respectively. Repeated clonotypes were defined using the "strict" criteria in scRepertoire as cells sharing the VDJC segments of both *Tcra* and *Tcrb* with identical *Cdr3* sequences at the nucleotide level. Clonal overlap scores, defined by scRepertoire as the intersection size of clonotypes between two populations divided by the length of the smallest one, were calculated using the clonalOverlap() function.

RNA-seq library preparation, sequencing and data processing—Cells were double-sorted using MoFlo Astrios or BD Aria II into TCL buffer (Qiagen) containing 1% 2-mercaptoethanol (2-ME, Sigma-Aldrich). For whole-muscle RNA-seq, total RNAs were isolated from TA muscles using TRIzol (Invitrogen) according to the manufacturer's instructions. Total RNAs were isolated from liver samples using Rneasy Lipid Tissue Mini Kit (Qiagen). Two nanograms of RNA were suspended in 5 μL of TCL+1% 2-ME. Libraries were constructed, sequenced, and the data was processed according to the Immgen protocol (https://www.immgen.org/img/Protocols/ImmGenULI_RNAseq_methods.pdf), and as previously described[43]. Subsequent normalization of raw read counts was performed in the Bioconductor package DESeq2 using the median of ratios method. Batch effects were removed using the removeBatchEffect() function in the *limma* package. Following normalization, GCT and CLS files were generated and used for downstream analysis. After normalization, reads were further filtered by minimal expression and coefficient of variation in Multiplot Studio (GenePattern; Broad Institute).

Analysis of bulk RNA-seq data—Gene expression dynamics in PBS- and rIL-17A-treated MuSCs time-series data were assessed using a two-step regression modeling strategy implemented with maSigPro[93]. An alpha of 0.05 was used to account for multiple hypothesis testing and a false discovery rate of 5% was applied to first identify differentially expressed transcripts. To identify co-expression clusters (or modules) during the time-series, silhouette analysis partitioned differential genes into 15 clusters (cluster correlation, r2>0.65). Clusters were visualized using Morpheus (Broad Institute). For gene signature scoring, the normalized gene-expression matrix was log-transformed and the z-score of each gene was calculated. This matrix was used to calculate normalized gene-expression scores for each module using the score_genes function in the scanpy package in python. The annotated list of gene modules was obtained from a previously published study that identified transcriptional changes during muscle injury[44]. Volcano and FC/FC plots were generated using Multiplot Studio (Broad Institute). Pathway analysis of differentially expressed genes between classes of samples was performed using Metascape and Enrichr.

Analysis of intestinal permeability—Mice were fasted for 4 hr before oral gavage with 150 μl of 25 mg/ml 4 kDa FITC-dextran (Chondrex). Blood samples were collected after 4 hr, allowed to clot at room temperature for 30 min, and serum was isolated by centrifugation at 2000 g for 15 min. FITC fluorescent signal in the serum was measured on a BioTek Synergy Mx Microplate Reader.

Histology—TA muscles and livers were collected and fixed in 10% formalin. Tissues were processed at the Rodent Histopathology Core at Harvard Medical School for hematoxylin and eosin (for muscle fiber size analysis) and picrosirius red (for fibrosis) staining. Four muscle sections, 200 μm apart, were recovered and stained for analysis. Images were acquired with a Nikon Ti inverted microscope. Efficiency of muscle repair was assessed histologically, as previously described[26,43,94]. In brief, we first identified the section from each sample with the largest number of regenerating muscle fibers (centrally nucleated fibers). For 4–5 representative regions in each of these sections, the cross-sectional area of individual muscle fibers was calculated by manually tracing the fiber circumference using ImageJ 1.53c[95]. Approximately 1,000 fibers were traced per sample. To assess fibrosis, the fraction of Picrosirius-Red-stained area in TA muscle and liver sections was determined using ImageJ 1.53c.

MuSC functional assays—MuSCs ($CD31^{-}CD45^{-}Sca1^{-}Vcam1^{+}$) were sorted from hindlimb muscle using a BD FACSAria II cell sorter. For the 5-Ethynyl-2′-deoxyuridine (EdU) incorporation assay, freshly sorted MuSCs were cultured in Ham's F10 with 10% horse serum and 1% penicillin-streptomycin (P/S) supplemented with 100ng/ml rIL-17A (Peprotech) for 36 h followed by a 4 h pulse with 10uM EdU. For the differentiation assay, freshly sorted MuSCs were cultured in Ham's F10 with 10% horse serum and 1% P/S supplemented with 100 ng/ml rIL-17A. The medium was changed every 2 days. Cultured cells were fixed in 4% paraformaldehyde for 5 min, washed with 0.1% PBS with Tween (PBST), permeabilized by 0.5% PBST for 20 min and then blocked with 4% IgG-free bovine serum albumin in PBST for 1 h. Samples were incubated with mouse anti-MyoG (clone F5D, Santa Cruz) or mouse anti-MyHC (Clone MF20, R&D) antibodies at 4°C overnight, washed 3 times, followed by incubation with Cy-3 donkey anti-Mouse secondary antibody (Jackson ImmunoResearch) for 1 h. The nuclei were counterstained with 100 ng/ml 4',6-diamidino-2-phenylindole (DAPI). After 3 washes, the samples were mounted and observed under a fluorescence microscope. The EdU staining was performed using a Click-iT™ imaging kit (Thermo Fisher Scientific). Images were acquired with a Nikon Ti inverted microscope. Image analysis was done using ImageJ 1.53c.

Measurement of liver transaminases—Blood samples were collected in EDTA-coated tubes and plasma was isolated by centrifugation at 2000 g for 15 min. Concentrations of plasma alanine transaminase and aspartate transaminase were analyzed on the Siemens Chemistry XPT clinical analyzer.

QUANTIFICATION AND STATISTICAL ANALYSIS

Statistical analyses were performed using GraphPad Prism software. Data were routinely presented as mean ± SEM. Statistical significance was calculated by unpaired Student's t-test (two-tailed), t-test of weighted sums, Kruskal-Wallis test, one-way or two-way ANOVA. P-values for gene-signature enrichment either up or down between a pairwise comparison in volcano and FC/FC plots were determined using the $\chi 2$ test. Statistical significance is denoted as the following: *$p<0.05$, **$p<0.01$, ***$p<0.001$.

Supplementary Material

Refer to Web version on PubMed Central for supplementary material.

ACKNOWLEDGEMENTS:

We thank K. Hattori, A. Ortiz-Lopez, L. Yang, O. Yaghi, P.K. Langston, D. Ramanan, T. Jayewickreme, Y. Zhu and X. Chi for experimental assistance; B. Vijaykumar for bioinformatics; C. Laplace for graphics; the Harvard Medical School (HMS) Rodent Histopathology Core; and the HMS Immunology Department Flow-Cytometry Core. This work was funded by grants from the NIH (R01 AR070334), the JPB Foundation, and Pfizer, Inc. to D.M. B.S.H. was partially supported by a Deutsche Forschungsgemeinschaft fellowship (HA 8510/1) and S.G.P. by an EMBO Long-term Fellowship (ACTF 547–2019).

REFERENCES

1. Muñoz-Rojas AR and Mathis D (2021). Tissue regulatory T cells: regulatory chameleons. Nat Rev Immunol 21, 597–611. [PubMed: 33772242]
2. Feuerer M, Herrero L, Cipolletta D, Naaz A, Wong J, Nayer A, Lee J, Goldfine AB, Benoist C, Shoelson S et al. (2009). Lean, but not obese, fat is enriched for a unique population of regulatory T cells that affect metabolic parameters. Nat Med 15, 930–939. [PubMed: 19633656]
3. Sefik E, Geva-Zatorsky N, Oh S, Konnikova L, Zemmour D, McGuire AM, Burzyn D, Ortiz-Lopez A, Lobera M, Yang J et al. (2015). Individual intestinal symbionts induce a distinct population of RORγ$^+$ regulatory T cells. Science 349, 993–997. [PubMed: 26272906]
4. Ohnmacht C, Park JH, Cording S, Wing JB, Atarashi K, Obata Y, Gaboriau-Routhiau V, Marques R, Dulauroy S, Fedoseeva M et al. (2015). The microbiota regulates type 2 immunity through RORγ$^+$ T cells. Science 349, 989–993. [PubMed: 26160380]
5. Yang BH, Hagemann S, Mamareli P, Lauer U, Hoffmann U, Beckstette M, Fohse L, Prinz I, Pezoldt J, Suerbaum S et al. (2016). Foxp3$^+$ T cells expressing RORγt represent a stable regulatory T-cell effector lineage with enhanced suppressive capacity during intestinal inflammation. Mucosal. Immunol 9, 444–457. [PubMed: 26307665]
6. Arpaia N, Green JA, Moltedo B, Arvey A, Hemmers S, Yuan S, Treuting PM, and Rudensky AY (2015). A distinct function of regulatory T cells in tissue protection. Cell 162, 1078–1089. [PubMed: 26317471]
7. Burzyn D, Kuswanto W, Kolodin D, Shadrach JL, Cerletti M, Jang Y, Sefik E, Tan TG, Wagers AJ, Benoist C et al. (2013). A special population of regulatory T cells potentiates muscle repair. Cell 155, 1282–1295. [PubMed: 24315098]
8. Scharschmidt TC, Vasquez KS, Truong HA, Gearty SV, Pauli ML, Nosbaum A, Gratz IK, Otto M, Moon JJ, Liese J et al. (2015). A wave of regulatory T cells into neonatal skin mediates tolerance to commensal microbes. Immunity 43, 1011–1021. [PubMed: 26588783]
9. Ali N, Zirak B, Rodriguez RS, Pauli ML, Truong HA, Lai K, Ahn R, Corbin K, Lowe MM, Scharschmidt TC et al. (2017). Regulatory T cells in skin facilitate epithelial stem cell differentiation. Cell 169, 1119–1129. [PubMed: 28552347]
10. Mathur AN, Zirak B, Boothby IC, Tan M, Cohen JN, Mauro TM, Mehta P, Lowe MM, Abbas AK, Ali N et al. (2019). Treg-cell control of a CXCL5-IL-17 inflammatory axis promotes hair-follicle-stem-cell differentiation during skin-barrier repair. Immunity. 50, 655–667. [PubMed: 30893588]
11. Panduro M, Benoist C, and Mathis D (2018). T_{reg} cells limit IFN-γ production to control macrophage accrual and phenotype during skeletal muscle regeneration. Proc Natl Acad Sci U S A 115, E2585–E2593. [PubMed: 29476012]
12. Abdel-Gadir A, Stephen-Victor E, Gerber GK, Noval RM, Wang S, Harb H, Wang L, Li N, Crestani E, Spielman S et al. (2019). Microbiota therapy acts via a regulatory T cell MyD88/RORγt pathway to suppress food allergy. Nat Med 25, 1164–1174. [PubMed: 31235962]
13. Kim KS, Hong SW, Han D, Yi J, Jung J, Yang BG, Lee JY, Lee M, and Surh CD (2016). Dietary antigens limit mucosal immunity by inducing regulatory T cells in the small intestine. Science 351, 858–863. [PubMed: 26822607]

14. Xu M, Pokrovskii M, Ding Y, Yi R, Au C, Harrison OJ, Galan C, Belkaid Y, Bonneau R, and Littman DR (2018). c-MAF-dependent regulatory T cells mediate immunological tolerance to a gut pathobiont. Nature 554, 373–377. [PubMed: 29414937]
15. Neumann C, Blume J, Roy U, Teh PP, Vasanthakumar A, Beller A, Liao Y, Heinrich F, Arenzana TL, Hackney JA et al. (2019). c-Maf-dependent Treg cell control of intestinal TH17 cells and IgA establishes host-microbiota homeostasis. Nat Immunol 20, 471–481. [PubMed: 30778241]
16. Al Nabhani Z, Dulauroy S, Marques R, Cousu C, Al BS, Dejardin F, Sparwasser T, Berard M, Cerf-Bensussan N, and Eberl G (2019). A weaning reaction to microbiota is required for resistance to immunopathologies in the adult. Immunity 50, 1276–1288. [PubMed: 30902637]
17. Mazmanian SK, Liu CH, Tzianabos AO, and Kasper DL (2005). An immunomodulatory molecule of symbiotic bacteria directs maturation of the host immune system. Cell 122, 107–118. [PubMed: 16009137]
18. Wu HJ, Ivanov II, Darce J, Hattori K, Shima T, Umesaki Y, Littman DR, Benoist C, and Mathis D (2010). Gut-residing segmented filamentous bacteria drive autoimmune arthritis via T helper 17 cells. Immunity. 32, 815–827. [PubMed: 20620945]
19. Ichinohe T, Pang IK, Kumamoto Y, Peaper DR, Ho JH, Murray TS, and Iwasaki A (2011). Microbiota regulates immune defense against respiratory tract influenza A virus infection. Proc Natl Acad Sci U S A 108, 5354–5359. [PubMed: 21402903]
20. Kim S, Kim H, Yim YS, Ha S, Atarashi K, Tan TG, Longman RS, Honda K, Littman DR, Choi GB et al. (2017). Maternal gut bacteria promote neurodevelopmental abnormalities in mouse offspring. Nature 549, 528–532. [PubMed: 28902840]
21. Mager LF, Burkhard R, Pett N, Cooke NCA, Brown K, Ramay H, Paik S, Stagg J, Groves RA, Gallo M et al. (2020). Microbiome-derived inosine modulates response to checkpoint inhibitor immunotherapy. Science 369, 1481–1489. [PubMed: 32792462]
22. Ivanov II, Atarashi K, Manel N, Brodie EL, Shima T, Karaoz U, Wei D, Goldfarb KC, Santee CA, Lynch SV et al. (2009). Induction of intestinal Th17 cells by segmented filamentous bacteria. Cell 139, 485–498. [PubMed: 19836068]
23. Gauguet S, D'Ortona S, Ahnger-Pier K, Duan B, Surana NK, Lu R, Cywes-Bentley C, Gadjeva M, Shan Q, Priebe GP et al. (2015). Intestinal microbiota of mice influences resistance to staphylococcus aureus pneumonia. Infect. Immun. 83, 4003–4014. [PubMed: 26216419]
24. McAleer JP, Nguyen NL, Chen K, Kumar P, Ricks DM, Binnie M, Armentrout RA, Pociask DA, Hein A, Yu A et al. (2016). Pulmonary Th17 antifungal immunity is regulated by the gut microbiome. J Immunol 197, 97–107. [PubMed: 27217583]
25. Tidball JG (2017). Regulation of muscle growth and regeneration by the immune system. Nat Rev Immunol 17, 165–178. [PubMed: 28163303]
26. Kuswanto W, Burzyn D, Panduro M, Wang KK, Jang YC, Wagers AJ, Benoist C, and Mathis D (2016). Poor repair of skeletal muscle in aging mice reflects a defect in local, interleukin-33-dependent accumulation of regulatory T cells. Immunity 44, 355–367. [PubMed: 26872699]
27. Wang K, Yaghi OK, Spallanzani RG, Chen X, Zemmour D, Lai N, Chiu IM, Benoist C, and Mathis D (2020). Neuronal, stromal, and T-regulatory cell crosstalk in murine skeletal muscle. Proc. Natl. Acad. Sci. U. S. A 117, 5402–5408. [PubMed: 32102913]
28. Dispirito JR, Zemmour D, Ramanan D, Cho J, Zilionis R, Klein AM, Benoist C, and Mathis D (2018). Molecular diversification of regulatory T cells in nonlymphoid tissues. Sci Immunol 3, eaat5861. [PubMed: 30217811]
29. Komatsu N, Mariotti-Ferrandiz ME, Wang Y, Malissen B, Waldmann H, and Hori S (2009). Heterogeneity of natural Foxp3+ T cells: a committed regulatory T-cell lineage and an uncommitted minor population retaining plasticity. Proc. Natl. Acad. Sci. U. S. A 106, 1903–1908. [PubMed: 19174509]
30. Tomura M, Yoshida N, Tanaka J, Karasawa S, Miwa Y, Miyawaki A, and Kanagawa O (2008). Monitoring cellular movement in vivo with photoconvertible fluorescence protein "Kaede" transgenic mice. Proc Natl Acad Sci U S A 105, 10871–10876. [PubMed: 18663225]
31. Morton AM, Sefik E, Upadhyay R, Weissleder R, Benoist C, and Mathis D (2014). Endoscopic photoconversion reveals unexpectedly broad leukocyte trafficking to and from the gut. Proc Natl Acad Sci U S A 111, 6696–6701. [PubMed: 24753589]

32. Borcherding N, Bormann NL, and Kraus G (2020). scRepertoire: an R-based toolkit for single-cell immune receptor analysis. F1000Res. 9, 47. [PubMed: 32789006]
33. Fonseca R, Beura LK, Quarnstrom CF, Ghoneim HE, Fan Y, Zebley CC, Scott MC, Fares-Frederickson NJ, Wijeyesinghe S, Thompson EA et al. (2020). Developmental plasticity allows outside-in immune responses by resident memory T cells. Nat Immunol 21, 412–421. [PubMed: 32066954]
34. Laidlaw BJ, Gray EE, Zhang Y, Ramirez-Valle F, and Cyster JG (2019). Sphingosine-1-phosphate receptor 2 restrains egress of γδ T cells from the skin. J. Exp. Med 216, 1487–1496. [PubMed: 31160320]
35. Ataide MA, Knopper K, Cruz de CP, Ugur M, Eickhoff S, Zou M, Shaikh H, Trivedi A, Grafen A, Yang T et al. (2022). Lymphatic migration of unconventional T cells promotes site-specific immunity in distinct lymph nodes. Immunity.
36. Kunkel GT, Maceyka M, Milstien S, and Spiegel S (2013). Targeting the sphingosine-1-phosphate axis in cancer, inflammation and beyond. Nat. Rev. Drug Discov. 12, 688–702. [PubMed: 23954895]
37. Lu H, Huang D, Ransohoff RM, and Zhou L (2011). Acute skeletal muscle injury: CCL2 expression by both monocytes and injured muscle is required for repair. FASEB J 25, 3344–3355. [PubMed: 21697550]
38. Giannakis N, Sansbury BE, Patsalos A, Hays TT, Riley CO, Han X, Spite M, and Nagy L (2019). Publisher Correction: Dynamic changes to lipid mediators support transitions among macrophage subtypes during muscle regeneration. Nat Immunol 20, 765–767.
39. Kolodin D, van PN, Li C, Magnuson AM, Cipolletta D, Miller CM, Wagers A, Germain RN, Benoist C, and Mathis D (2015). Antigen- and cytokine-driven accumulation of regulatory T cells in visceral adipose tissue of lean mice. Cell Metab 21, 543–557. [PubMed: 25863247]
40. Li C, Dispirito JR, Zemmour D, Spallanzani RG, Kuswanto W, Benoist C, and Mathis D (2018). TCR transgenic mice reveal stepwise, multi-site acquisition of the distinctive fat-Treg phenotype. Cell 174, 285–299. [PubMed: 29887374]
41. Cho J, Kuswanto W, Benoist C, and Mathis D (2019). T cell receptor specificity drives accumulation of a reparative population of regulatory T cells within acutely injured skeletal muscle. Proc Natl Acad Sci U S A 116, 26727–26733. [PubMed: 31822623]
42. Akagbosu B, Tayyebi Z, Shibu G, Paucar Iza YA, Deep D, Parisotto YF, Fisher L, Pasolli HA, Thevin V, Elmentaite R et al. (2022). Novel antigen presenting cell imparts Treg-dependent tolerance to gut microbiota. Nature.
43. Mann AO, Hanna BS, Munoz-Rojas AR, Sandrock I, Prinz I, Benoist C, and Mathis D (2022). IL-17A-producing γδT cells promote muscle regeneration in a microbiota-dependent manner. J Exp Med 219, e20211504. [PubMed: 35380608]
44. Aguilar CA, Shcherbina A, Ricke DO, Pop R, Carrigan CT, Gifford CA, Urso ML, Kottke MA, and Meissner A (2015). In vivo monitoring of transcriptional dynamics after lower-limb muscle injury enables quantitative classification of healing. Sci Rep 5, 13885. [PubMed: 26381351]
45. Arnold L, Henry A, Poron F, Baba-Amer Y, van RN, Plonquet A, Gherardi RK, and Chazaud B (2007). Inflammatory monocytes recruited after skeletal muscle injury switch into antiinflammatory macrophages to support myogenesis. J Exp. Med 204, 1057–1069. [PubMed: 17485518]
46. Cheng M, Nguyen MH, Fantuzzi G, and Koh TJ (2008). Endogenous interferon-gamma is required for efficient skeletal muscle regeneration. Am. J Physiol Cell Physiol 294, C1183–C1191. [PubMed: 18353892]
47. Chen SE, Jin B, and Li YP (2007). TNF-alpha regulates myogenesis and muscle regeneration by activating p38 MAPK. Am. J Physiol Cell Physiol 292, C1660–C1671. [PubMed: 17151142]
48. Londhe P and Davie JK (2011). Gamma interferon modulates myogenesis through the major histocompatibility complex class II transactivator, CIITA. Mol Cell Biol. 31, 2854–2866. [PubMed: 21576360]
49. Londhe P and Davie JK (2013). Interferon-gamma resets muscle cell fate by stimulating the sequential recruitment of JARID2 and PRC2 to promoters to repress myogenesis. Sci Signal. 6, ra107. [PubMed: 24327761]

50. Oprescu SN, Yue F, Qiu J, Brito LF, and Kuang S (2020). Temporal dynamics and heterogeneity of cell populations during skeletal muscle regeneration. iScience. 23, 100993. [PubMed: 32248062]
51. Sambasivan R, Yao R, Kissenpfennig A, Van WL, Paldi A, Gayraud-Morel B, Guenou H, Malissen B, Tajbakhsh S, and Galy A (2011). Pax7-expressing satellite cells are indispensable for adult skeletal muscle regeneration. Development 138, 3647–3656. [PubMed: 21828093]
52. Lepper C, Partridge TA, and Fan CM (2011). An absolute requirement for Pax7-positive satellite cells in acute injury-induced skeletal muscle regeneration. Development 138, 3639–3646. [PubMed: 21828092]
53. Girgenrath M, Weng S, Kostek CA, Browning B, Wang M, Brown SA, Winkles JA, Michaelson JS, Allaire N, Schneider P et al. (2006). TWEAK, via its receptor Fn14, is a novel regulator of mesenchymal progenitor cells and skeletal muscle regeneration. EMBO J 25, 5826–5839. [PubMed: 17124496]
54. Yartseva V, Goldstein LD, Rodman J, Kates L, Chen MZ, Chen YJ, Foreman O, Siebel CW, Modrusan Z, Peterson AS et al. (2020). Heterogeneity of satellite cells implicates DELTA1/NOTCH2 signaling in self-renewal. Cell Rep 30, 1491–1503. [PubMed: 32023464]
55. Rodgers JT, King KY, Brett JO, Cromie MJ, Charville GW, Maguire KK, Brunson C, Mastey N, Liu L, Tsai CR et al. (2014). mTORC1 controls the adaptive transition of quiescent stem cells from G_0 to G_{Alert}. Nature 510, 393–396. [PubMed: 24870234]
56. Kocic J, Santibanez JF, Krstic A, Mojsilovic S, Dordevic IO, Trivanovic D, Ilic V, and Bugarski D (2012). Interleukin 17 inhibits myogenic and promotes osteogenic differentiation of C2C12 myoblasts by activating ERK1,2. Biochim. Biophys. Acta 1823, 838–849. [PubMed: 22285818]
57. Xia N, Lu Y, Gu M, Li N, Liu M, Jiao J, Zhu Z, Li J, Li D, Tang T et al. (2020). A unique population of regulatory T cells in heart potentiates cardiac protection from myocardial infarction. Circulation 142, 1956–1973. [PubMed: 32985264]
58. Wang R, Tang R, Li B, Ma X, Schnabl B, and Tilg H (2021). Gut microbiome, liver immunology, and liver diseases. Cell Mol. Immunol 18, 4–17. [PubMed: 33318628]
59. Li F, Hao X, Chen Y, Bai L, Gao X, Lian Z, Wei H, Sun R, and Tian Z (2017). The microbiota maintain homeostasis of liver-resident γδT-17 cells in a lipid antigen/CD1d-dependent manner. Nat. Commun. 7, 13839. [PubMed: 28067223]
60. Gomes AL, Teijeiro A, Buren S, Tummala KS, Yilmaz M, Waisman A, Theurillat JP, Perna C, and Djouder N (2016). Metabolic inflammation-associated IL-17A causes non-alcoholic steatohepatitis and hepatocellular carcinoma. Cancer Cell 30, 161–175. [PubMed: 27411590]
61. Matsumoto M, Hada N, Sakamaki Y, Uno A, Shiga T, Tanaka C, Ito T, Katsume A, and Sudoh M (2013). An improved mouse model that rapidly develops fibrosis in non-alcoholic steatohepatitis. Int. J Exp Pathol. 94, 93–103. [PubMed: 23305254]
62. Meng F, Wang K, Aoyama T, Grivennikov SI, Paik Y, Scholten D, Cong M, Iwaisako K, Liu X, Zhang M et al. (2012). Interleukin-17 signaling in inflammatory, Kupffer cells, and hepatic stellate cells exacerbates liver fibrosis in mice. Gastroenterology 143, 765–776. [PubMed: 22687286]
63. Wucherpfennig KW and Strominger JL (1995). Molecular mimicry in T cell-mediated autoimmunity: viral peptides activate human T cell clones specific for myelin basic protein. Cell 80, 695–705. [PubMed: 7534214]
64. Harkiolaki M, Holmes SL, Svendsen P, Gregersen JW, Jensen LT, McMahon R, Friese MA, van BG, Etzensperger R, Tzartos JS et al. (2009). T cell-mediated autoimmune disease due to low-affinity crossreactivity to common microbial peptides. Immunity. 30, 348–357. [PubMed: 19303388]
65. Szymula A, Rosenthal J, Szczerba BM, Bagavant H, Fu SM, and Deshmukh US (2014). T cell epitope mimicry between Sjögren's syndrome Antigen A (SSA)/Ro60 and oral, gut, skin and vaginal bacteria. Clin Immunol 152, 1–9. [PubMed: 24576620]
66. Pianta A, Arvikar SL, Strle K, Drouin EE, Wang Q, Costello CE, and Steere AC (2017). Two rheumatoid arthritis-specific autoantigens correlate microbial immunity with autoimmune responses in joints. J Clin Invest 127, 2946–2956. [PubMed: 28650341]
67. Hebbandi Nanjundappa R, Ronchi F, Wang J, Clemente-Casares X, Yamanouchi J, Sokke UC, Yang Y, Blanco J, Bassolas-Molina H, Salas A et al. (2017). A gut microbial mimic that hijacks diabetogenic autoreactivity to suppress colitis. Cell 171, 655–667. [PubMed: 29053971]

68. Carrasco Pro S, Lindestam Arlehamn CS, Dhanda SK, Carpenter C, Lindvall M, Faruqi AA, Santee CA, Renz H, Sidney J, Peters B et al. (2018). Microbiota epitope similarity either dampens or enhances the immunogenicity of disease-associated antigenic epitopes. PLoS One 13, e0196551. [PubMed: 29734356]
69. Garabatos N and Santamaria P (2022). Gut microbial antigenic mimicry in autoimmunity. Front Immunol 13, 873607. [PubMed: 35572569]
70. Seo BR, Payne CJ, McNamara SL, Freedman BR, Kwee BJ, Nam S, de L,I, Darnell M, Alvarez JT, Dellacherie MO et al. (2021). Skeletal muscle regeneration with robotic actuation-mediated clearance of neutrophils. Sci Transl. Med 13, eabe8868. [PubMed: 34613813]
71. Zhao J, Chen X, Herjan T, and Li X (2020). The role of interleukin-17 in tumor development and progression. J. Exp. Med 217.
72. Chen X, Cai G, Liu C, Zhao J, Gu C, Wu L, Hamilton TA, Zhang CJ, Ko J, Zhu L et al. (2019). IL-17R-EGFR axis links wound healing to tumorigenesis in Lrig1^{+} stem cells. J. Exp. Med 216, 195–214. [PubMed: 30578323]
73. Wu L, Chen X, Zhao J, Martin B, Zepp JA, Ko JS, Gu C, Cai G, Ouyang W, Sen G et al. (2015). A novel IL-17 signaling pathway controlling keratinocyte proliferation and tumorigenesis via the TRAF4-ERK5 axis. J. Exp. Med 212, 1571–1587. [PubMed: 26347473]
74. Zepp JA, Zhao J, Liu C, Bulek K, Wu L, Chen X, Hao Y, Wang Z, Wang X, Ouyang W et al. (2017). IL-17A-induced PLET1 expression contributes to tissue repair and colon tumorigenesis. J. Immunol. 199, 3849–3857. [PubMed: 29070673]
75. Huang H, Kim HJ, Chang EJ, Lee ZH, Hwang SJ, Kim HM, Lee Y, and Kim HH (2009). IL-17 stimulates the proliferation and differentiation of human mesenchymal stem cells: implications for bone remodeling. Cell Death. Differ. 16, 1332–1343. [PubMed: 19543237]
76. Kang Z, Wang C, Zepp J, Wu L, Sun K, Zhao J, Chandrasekharan U, DiCorleto PE, Trapp BD, Ransohoff RM et al. (2013). Act1 mediates IL-17-induced EAE pathogenesis selectively in NG2^{+} glial cells. Nat Neurosci. 16, 1401–1408. [PubMed: 23995070]
77. Kolodziejczyk AA, Zheng D, and Elinav E (2019). Diet-microbiota interactions and personalized nutrition. Nat Rev Microbiol. 17, 742–753. [PubMed: 31541197]
78. Liwinski T and Elinav E (2020). Harnessing the microbiota for therapeutic purposes. Am. J Transplant. 20, 1482–1488. [PubMed: 31858698]
79. Bettelli E, Carrier Y, Gao W, Korn T, Strom TB, Oukka M, Weiner HL, and Kuchroo VK (2006). Reciprocal developmental pathways for the generation of pathogenic effector TH17 and regulatory T cells. Nature 441, 235–238. [PubMed: 16648838]
80. Eberl G, Marmon S, Sunshine MJ, Rennert PD, Choi Y, and Littman DR (2004). An essential function for the nuclear receptor RORγt in the generation of fetal lymphoid tissue inducer cells. Nat. Immunol. 5, 64–73. [PubMed: 14691482]
81. Liston A, Nutsch KM, Farr AG, Lund JM, Rasmussen JP, Koni PA, and Rudensky AY (2008). Differentiation of regulatory Foxp3^{+} T cells in the thymic cortex. Proc Natl. Acad Sci U S. A. 105, 11903–11908. [PubMed: 18695219]
82. Kim JM, Rasmussen JP, and Rudensky AY (2007). Regulatory T cells prevent catastrophic autoimmunity throughout the lifespan of mice. Nat. Immunol 8, 191–197. [PubMed: 17136045]
83. Rubtsov YP, Rasmussen JP, Chi EY, Fontenot J, Castelli L, Ye X, Treuting P, Siewe L, Roers A, Henderson WR Jr. et al. (2008). Regulatory T cell-derived interleukin-10 limits inflammation at environmental interfaces. Immunity 28, 546–558. [PubMed: 18387831]
84. Wende H, Lechner SG, Cheret C, Bourane S, Kolanczyk ME, Pattyn A, Reuter K, Munier FL, Carroll P, Lewin GR et al. (2012). The transcription factor c-Maf controls touch receptor development and function. Science 335, 1373–1376. [PubMed: 22345400]
85. Hardy CL, Bhathal PS, Snibson KJ, and Adams TE (1997). Comparison of intrahepatic lymphocytes from normal and growth hormone transgenic mice with chronic hepatitis and liver cancer. Immunology 90, 412–420. [PubMed: 9155649]
86. Liu L, Cheung TH, Charville GW, and Rando TA (2015). Isolation of skeletal muscle stem cells by fluorescence-activated cell sorting. Nat. Protoc. 10, 1612–1624. [PubMed: 26401916]

87. Pratama A, Schnell A, Mathis D, and Benoist C (2020). Developmental and cellular age direct conversion of CD4$^+$ T cells into RORγ^+ or Helios$^+$ colon Treg cells. J Exp. Med 217, e20190428. [PubMed: 31685531]

88. Kiner E, Willie E, Vijaykumar B, Chowdhary K, Schmutz H, Chandler J, Schnell A, Thakore PI, LeGros G, Mostafavi S et al. (2021). Gut CD4$^+$ T cell phenotypes are a continuum molded by microbes, not by T_H archetypes. Nat. Immunol.

89. Li C, Muñoz-Rojas AR, Wang G, Mann AO, Benoist C, and Mathis D (2021). PPARγ marks splenic precursors of multiple nonlymphoid-tissue Treg compartments. Proc Natl Acad Sci U S A 118, e2025197118. [PubMed: 33753509]

90. Butler A, Hoffman P, Smibert P, Papalexi E, and Satija R (2018). Integrating single-cell transcriptomic data across different conditions, technologies, and species. Nat Biotechnol. 36, 411–420. [PubMed: 29608179]

91. Alquicira-Hernandez J and Powell JE (2021). Nebulosa recovers single cell gene expression signals by kernel density estimation. Bioinformatics.

92. Korsunsky I, Millard N, Fan J, Slowikowski K, Zhang F, Wei K, Baglaenko Y, Brenner M, Loh PR, and Raychaudhuri S (2019). Fast, sensitive and accurate integration of single-cell data with Harmony. Nat Methods 16, 1289–1296. [PubMed: 31740819]

93. Nueda MJ, Tarazona S, and Conesa A (2014). Next maSigPro: updating maSigPro bioconductor package for RNA-seq time series. Bioinformatics. 30, 2598–2602. [PubMed: 24894503]

94. Almada AE, Horwitz N, Price FD, Gonzalez AE, Ko M, Bolukbasi OV, Messemer KA, Chen S, Sinha M, Rubin LL et al. (2021). FOS licenses early events in stem cell activation driving skeletal muscle regeneration. Cell Rep 34, 108656. [PubMed: 33503437]

95. Schindelin J, Arganda-Carreras I, Frise E, Kaynig V, Longair M, Pietzsch T, Preibisch S, Rueden C, Saalfeld S, Schmid B et al. (2012). Fiji: an open-source platform for biological-image analysis. Nat Methods 9, 676–682. [PubMed: 22743772]

96. Geva-Zatorsky N, Sefik E, Kua L, Pasman L, Tan TG, Ortiz-Lopez A, Yanortsang TB, Yang L, Jupp R, Mathis D et al. (2017). Mining the human gut microbiota for immunomodulatory organisms. Cell 168, 928–943. [PubMed: 28215708]

97. Hao Y, Hao S, Andersen-Nissen E, Mauck WM III, Zheng S, Butler A, Lee MJ, Wilk AJ, Darby C, Zager M et al. (2021). Integrated analysis of multimodal single-cell data. Cell 184, 3573–3587. [PubMed: 34062119]

98. Trapnell C, Roberts A, Goff L, Pertea G, Kim D, Kelley DR, Pimentel H, Salzberg SL, Rinn JL, and Pachter L (2012). Differential gene and transcript expression analysis of RNA-seq experiments with TopHat and Cufflinks. Nat Protoc. 7, 562–578. [PubMed: 22383036]

99. Love MI, Huber W, and Anders S (2014). Moderated estimation of fold change and dispersion for RNA-seq data with DESeq2. Genome Biol. 15, 550. [PubMed: 25516281]

100. Ritchie ME, Phipson B, Wu D, Hu Y, Law CW, Shi W, and Smyth GK (2015). limma powers differential expression analyses for RNA-sequencing and microarray studies. Nucleic Acids Res. 43, e47. [PubMed: 25605792]

101. Wolf FA, Angerer P, and Theis FJ (2018). SCANPY: large-scale single-cell gene expression data analysis. Genome Biol. 19, 15. [PubMed: 29409532]

102. Zhou Y, Zhou B, Pache L, Chang M, Khodabakhshi AH, Tanaseichuk O, Benner C, and Chanda SK (2019). Metascape provides a biologist-oriented resource for the analysis of systems-level datasets. Nat. Commun. 10, 1523. [PubMed: 30944313]

103. Kuleshov MV, Jones MR, Rouillard AD, Fernandez NF, Duan Q, Wang Z, Koplev S, Jenkins SL, Jagodnik KM, Lachmann A et al. (2016). Enrichr: a comprehensive gene set enrichment analysis web server 2016 update. Nucleic Acids Res. 44, W90–W97. [PubMed: 27141961]

HIGHLIGHTS

- Muscle injury induces local accumulation of RORγ+ Treg cells emanating from the gut.
- The microbiota regulates muscle repair via RORγ+ Treg cells.
- Muscle RORγ+ Treg cells shield differentiating muscle stem cells from IL-17.
- RORγ+ Treg cell emissaries play a general role in the homeostasis of extra-gut tissues.

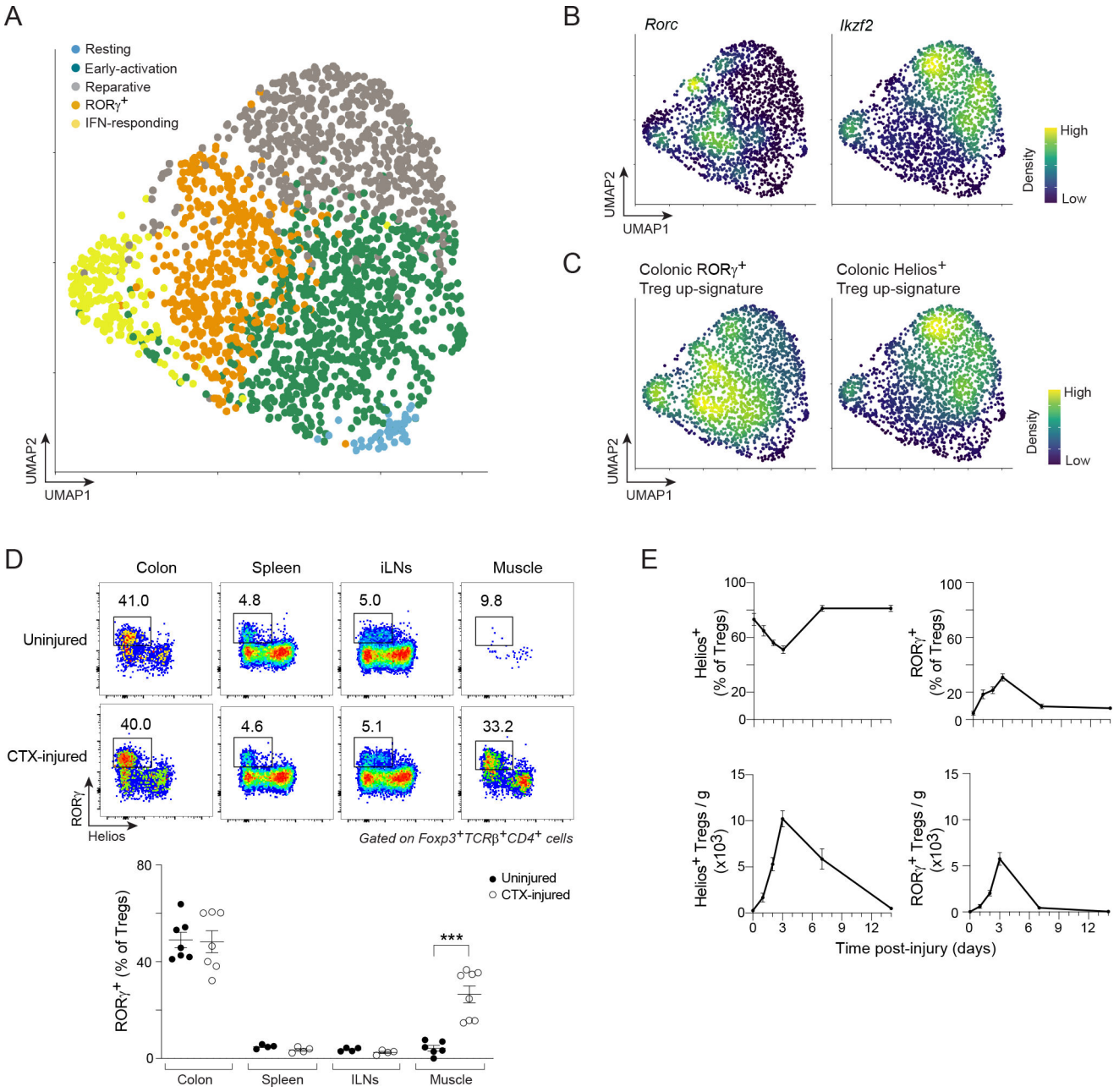

Figure 1: Accumulation of RORγ$^+$ Treg cells in skeletal muscle early after acute injury

(A–C) scRNA-seq of Treg cells from hindlimb muscles of *Foxp3^{GFP}* mice 3 days after CTX-induced injury. A) 2D UMAP plot. B, C) Density plots of the expression of the indicated genes and signatures. (D) Flow-cytometry of RORγ$^+$ Treg cells at steady-state and 3 days after CTX-induced injury. Upper panel: representative dot-plots (2–3 independent experiments); lower panel: summary data. (E) Time course of fractions (top) and numbers (bottom) of Helios$^+$ and RORγ$^+$ Treg cells in CTX-injured muscles. Unpaired t-test (D). See also Figure S1.

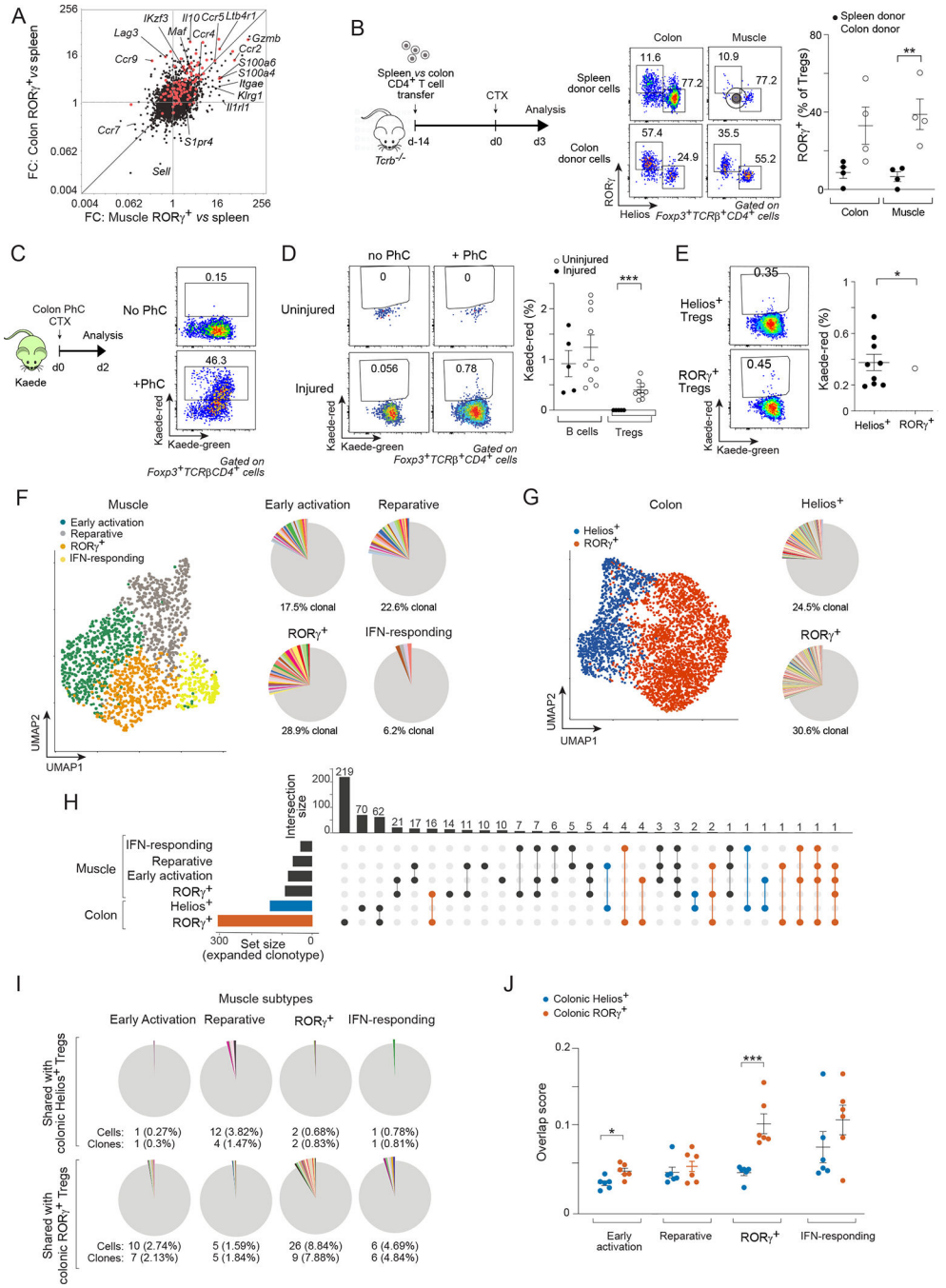

Figure 2: A colonic provenance for muscle RORγ$^+$ Treg cells

(A) Transcriptomic fold-change/fold-change (FC) plots comparing muscle RORγ$^+$ vs spleen Treg cells at day 4 after CTX-induced injury *vis-a-vis* colon RORγ$^+$ vs spleen Treg cells. Red: colonic RORγ$^+$ Treg up-signature. (B) Spleen or colon CD4$^+$ T cells were transferred into *Tcrb*$^{-/-}$ mice followed by CTX injection. Experimental design (left), representative dot-plots (middle), and summary data (right) of RORγ$^+$ Treg cells in colon and muscle. (C-E) Colonic photoconversion (PhC) of Kaede mice ± CTX-induced injury. C) Experimental design (left) and representative dot-plots (right) of colon PhC efficiency at day 0. D, E)

emigration of the indicated colonic cells to hindlimb muscles after 48 hr. Representative dot-plots (left) and summary data (right). (F-J) Paired scRNA-seq and sc *Tcr*-seq of muscle and colon Treg cells on day 3 after CTX injection. F) Left: UMAP of muscle data; right: pie-charts of sc *Tcr*-seq data showing the proportion of clonally expanded cells in each cluster. Different colors depict individual clones; non-expanded clones in gray. G) Same as panel F for colon Treg cells. H) Upset plot of intra-organ and inter-muscle-colon clonotype sharing. Set size indicates total number of expanded clones for each subtype. On top, the total number of shared clones is displayed. Incidences of clone sharing between any muscle Treg subtype and colonic RORγ^+ (red) or Helios$^+$ (blue) Treg cells are highlighted. I) Pie-charts depicting numbers and frequencies of clonotypes shared between muscle Treg cell subtypes and colonic RORγ^+ or Helios$^+$ Treg cells. Different colors depict individual clones; non-expanded clones in gray. J) Clonal overlap score between muscle Treg subtypes and colonic RORγ^+ *vs* Helios$^+$ Treg cells in individual mice. Representative dot-plots are from 2–3 independent experiments. Unpaired t-test (B, D), paired t-test (E), or two-way ANOVA (J). See also Figure S2.

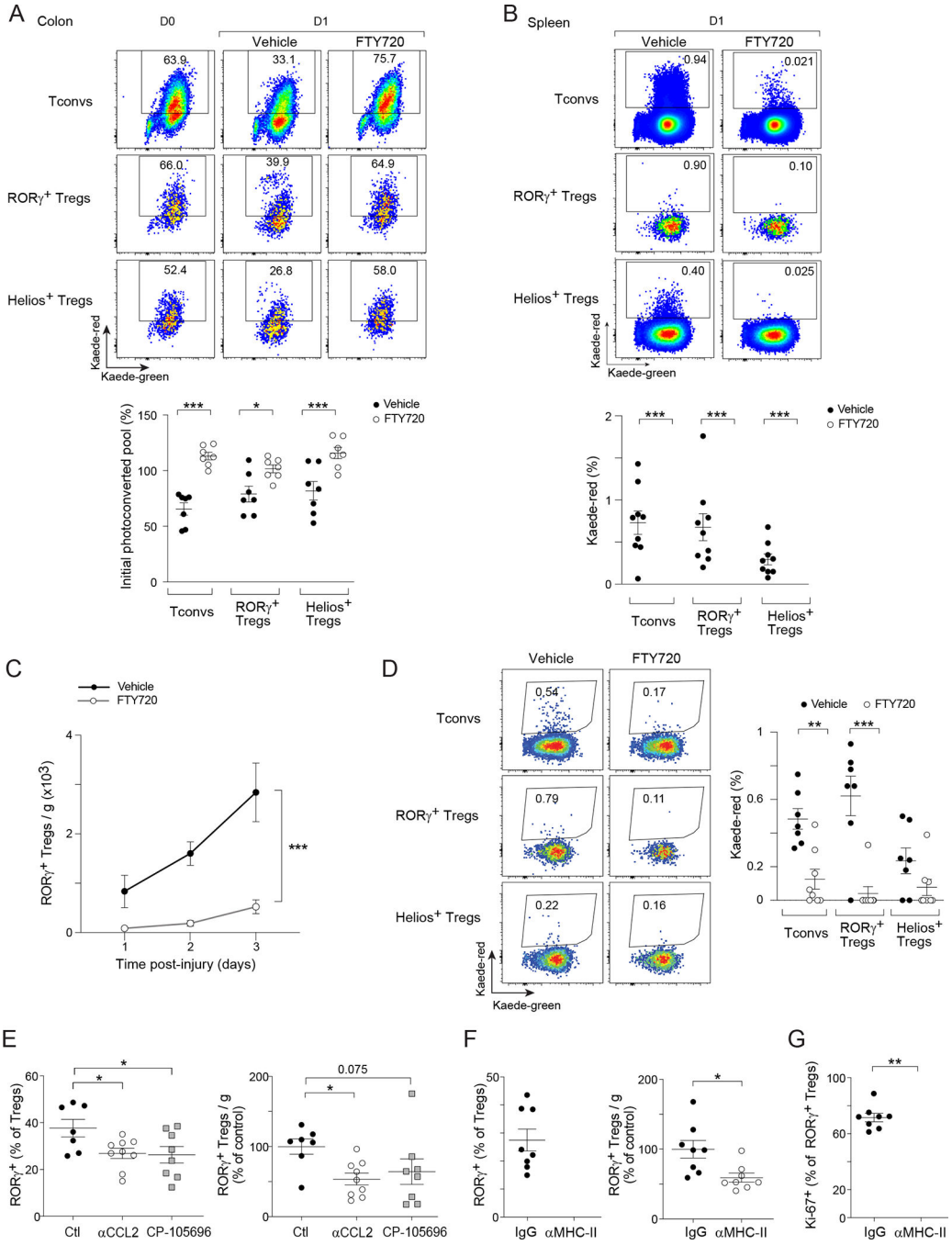

Figure 3: Mechanisms of RORγ$^+$ Treg cell accumulation in regenerating muscle

(A) Egress of diverse lymphocyte populations from the colon, and (B) their emigration to spleen after 24 hr of colonic PhC of Kaede mice. Top: representative dot-plots; bottom: summary data. (C) Muscle RORγ$^+$ Treg cell numbers after CTX-induced injury in vehicle- or FTY720-treated mice. (D) Colon PhC coupled with CTX-induced injury as per Figure 2C. Representative dot-plots (left) and summary data (right) of emigration of colonic cells to hindlimb muscles after 48 hr. (E) RORγ$^+$ Treg cell fraction (left) and number (right) in hindlimb muscles 2 days after CTX-induced injury in in control- (Ctl), αCCL2-, or

CP-105696-treated mice. (F, G) Mice were treated with isotype (IgG) or αMHC-II antibody. F) Muscle RORγ^+ Treg cell fraction (left) and number (right), and G) Ki-67 expression 3 days after CTX-induced injury. Representative dot-plots are from 2–3 independent experiments. Unpaired t-test (A, B, F, G), two-way ANOVA (C), or one-way ANOVA (E). See also Figure S3.

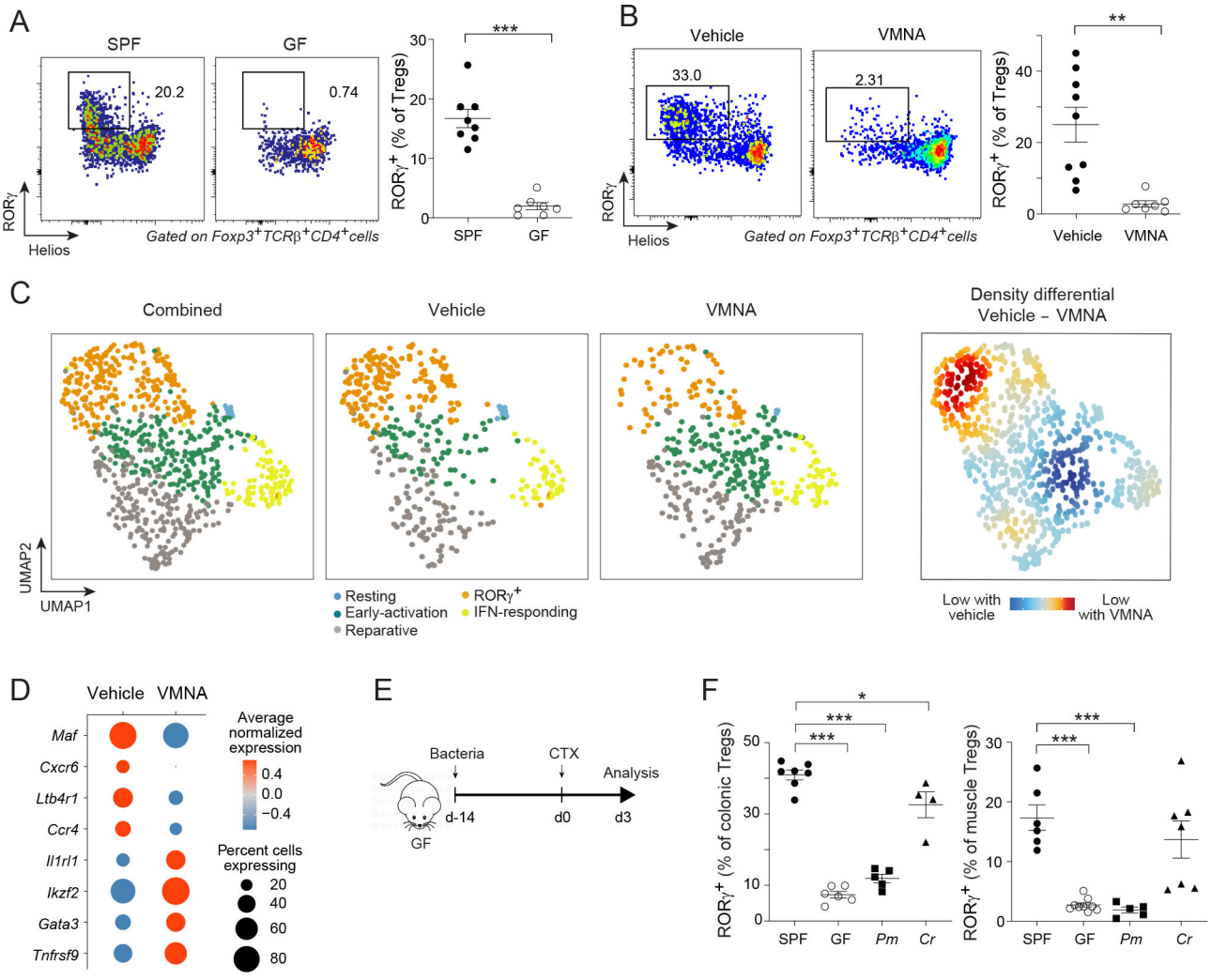

Figure 4: Microbiota-dependence of muscle RORγ$^+$ Treg cells

(A) Comparison of RORγ$^+$ Treg cells from hindlimb muscles 3 days after CTX-induced injury of specific-pathogen-free (SPF) or germ-free (GF) mice. Left: representative dot-plots (3 independent experiments); right: summary data. (B) Same as panel A except SPF mice were treated or not with the Abx cocktail, VMNA (vancomycin, metronidazole, neomycin, ampicillin). (C, D) scRNA-seq comparison of muscle Treg cells from vehicle- and VMNA-treated *Foxp3*^{GFP} mice 3 days after CTX-induced injury. C) 2D UMAP plot of the two conditions combined (left), each individual condition (middle) and their differential (right). (D) Bubble-plot of the average transcript expression of key marker genes in muscle Treg cells of vehicle- *vs* VMNA-treated mice. (E, F) Monocolonization. E) Experimental design: GF mice were orally gavaged with *Peptostreptococus magnus* (*Pm*) or *Clostridium ramosum* (*Cr*) before CTX-induced injury. F) RORγ$^+$ Treg cells in colonic lamina propria (left) or muscles (right). Unpaired t-test (A, B) or one-way ANOVA (F). See also Figure S4.

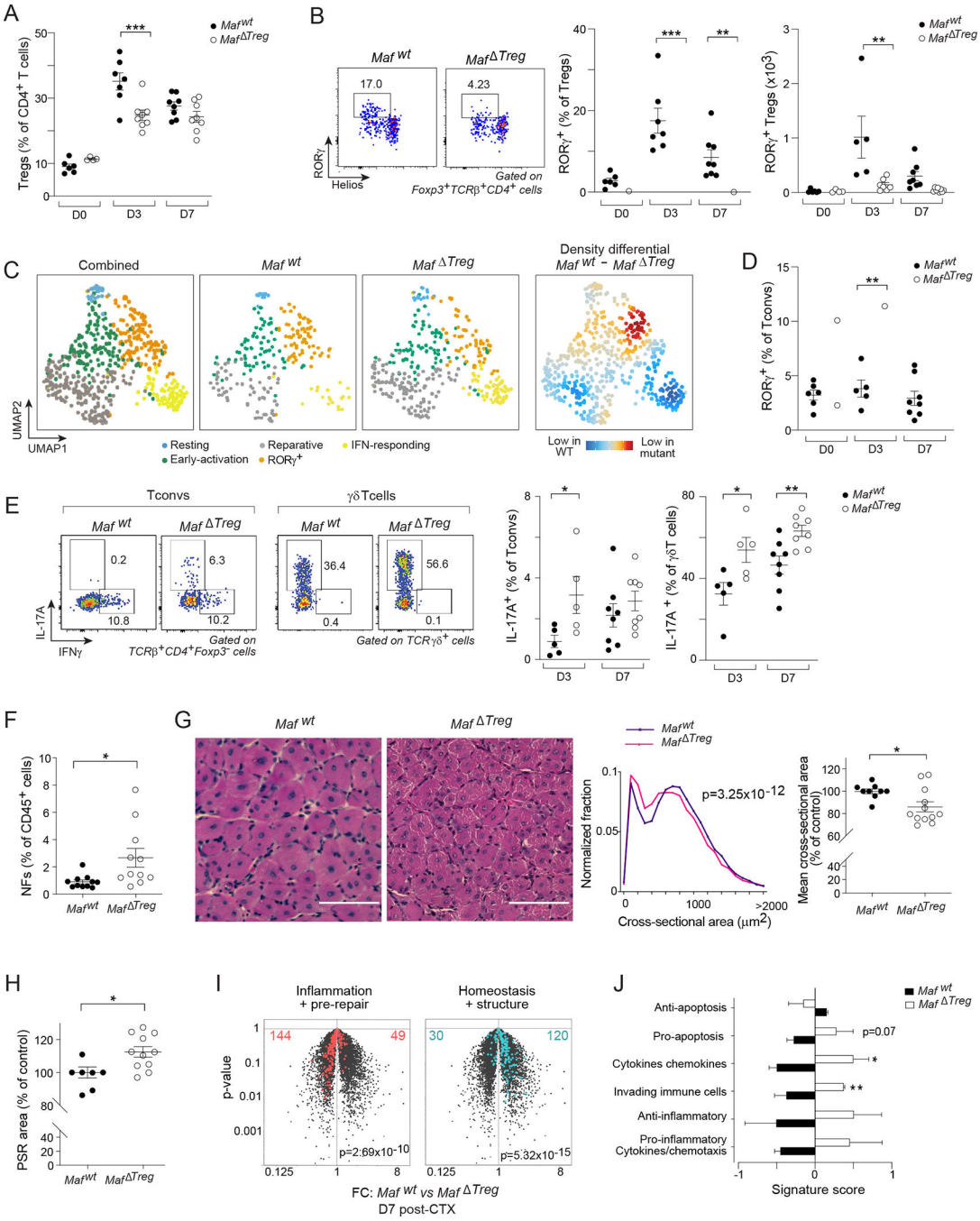

Figure 5: Impacts of RORγ$^+$ Treg cell depletion on immunocytes and tissue repair

Comparisons of hindlimb muscles from *Maf*^{wt} and *Maf*$^{\Delta Treg}$ littermates 0, 3, or 7 days after CTX-induced injury. Quantification of (A) Total, and B) RORγ$^+$ Treg cells. (C) scRNA-seq of muscle Treg cells 3 days after CTX-induced injury. 2D UMAP plot of combined data from the two genotypes (left); each individual condition (middle) and their differential (right). (D) Quantification of muscle RORγ$^+$CD4$^+$Foxp3$^-$ (Tconv) cells, and (E) production of IFNγ and IL-17A by Tconv and γδT cells. (F-J) Analysis of muscle repair efficiency 7 days after CTX-induced injury. F) Quantification of muscle neutrophils (NFs).

G) Representative images of H&E staining (left); distribution of cross-sectional areas of individual centrally nucleated fibers (middle); average fiber areas for individual mice (right). H) Quantification of fibrotic areas via picrosirius red (PSR) staining. (I, J) Transcriptional analyses of whole muscle (n=3). I) Volcano plot illustrating FC differences between the two genotypes. Repair-related signatures[43] are highlighted. J) Gene-signature scores of inflammatory gene sets[44]. Representative dot-plots and images are from 2–4 independent experiments. t-test of weighted sums (G middle), Chi-squared test (I), otherwise unpaired t-test. See also Figure S5.

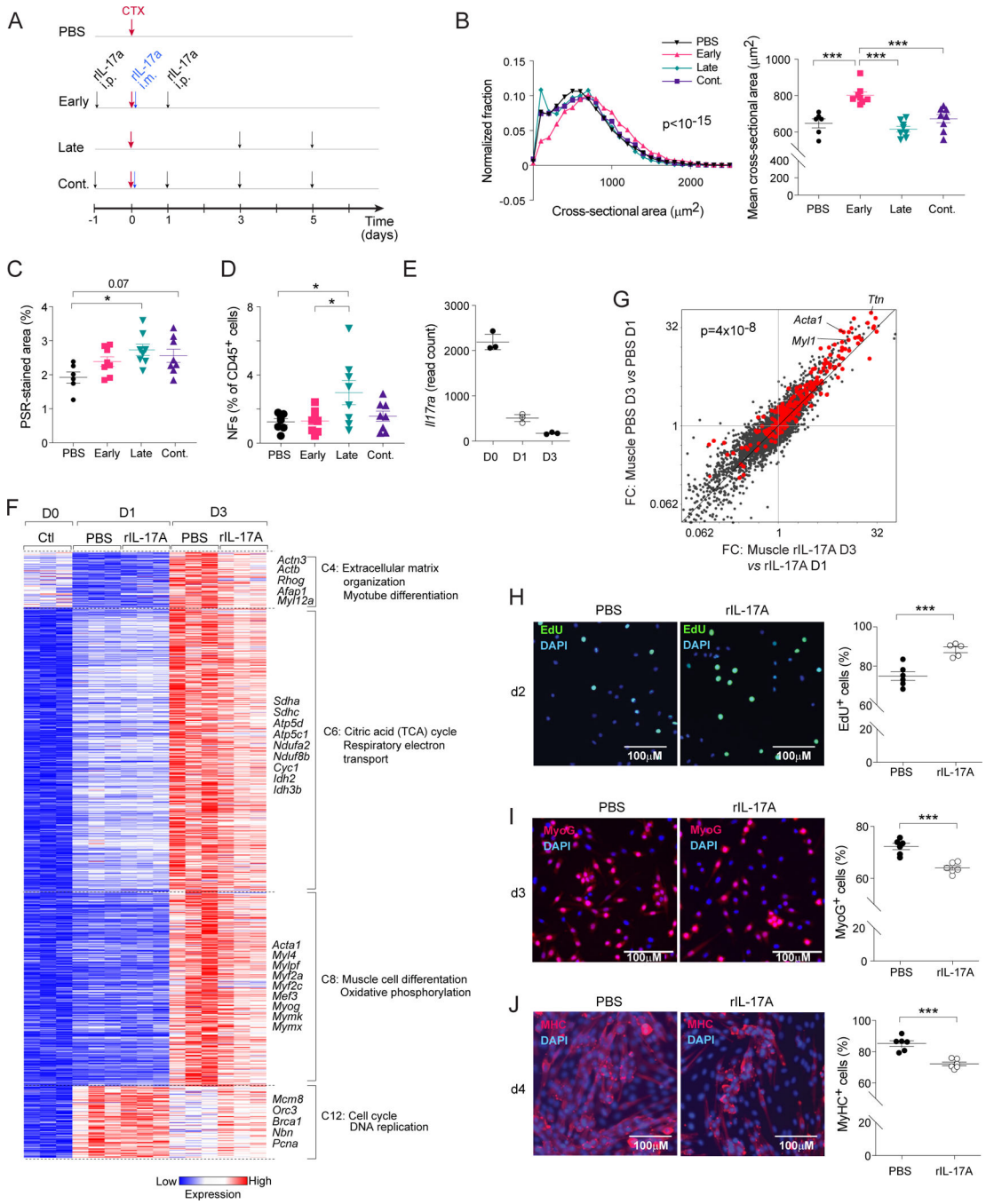

Figure 6: Impacts of IL-17A on muscle stem cells and repair

(A-D) B6 mice were treated with vehicle or rIL-17A early, late or continuously (cont.) after CTX-induced injury. Muscles were analyzed 7 days post-injury. A) Treatment schematic. B) Distribution of cross-sectional areas of individual centrally nucleated fibers (left), and average fiber areas for individual mice (right). C) Quantification of muscle fibrotic areas via PSR staining. D) Quantification of muscle NFs. (E-G) RNA-seq analysis of sorted MuSCs from PBS- or rIL-17A-treated mice on days 0, 1 and 3 after CTX-induced injury. Treatment schedule as per panel A. E) *Il17ra* transcript quantification. F) k-means clustering

of dynamically differential transcripts. Only select clusters are depicted. G) FC/FC plots for PBS- *vs* rIL-17A-treated mice on day 3 versus 1 after injury. MuSC differentiation signature genes[54] highlighted in red. (H-J) Freshly isolated MuSCs were cultured *in vitro* with or without rIL-17A. Representative images (left, 2–3 independent experiments) and summary data (right) of H) EdU incorporation, I) myogenin (MyoG), and J) Myosin Heavy Chain (MyHC) expression after 2, 3 and 4 days of culture, respectively. Kruskal-Wallis test (B left), Chi-squared test of the number of signature genes falling on either side of the diagonal (G), Unpaired t-test (H-J), otherwise one-way ANOVA. See also Figure S6.

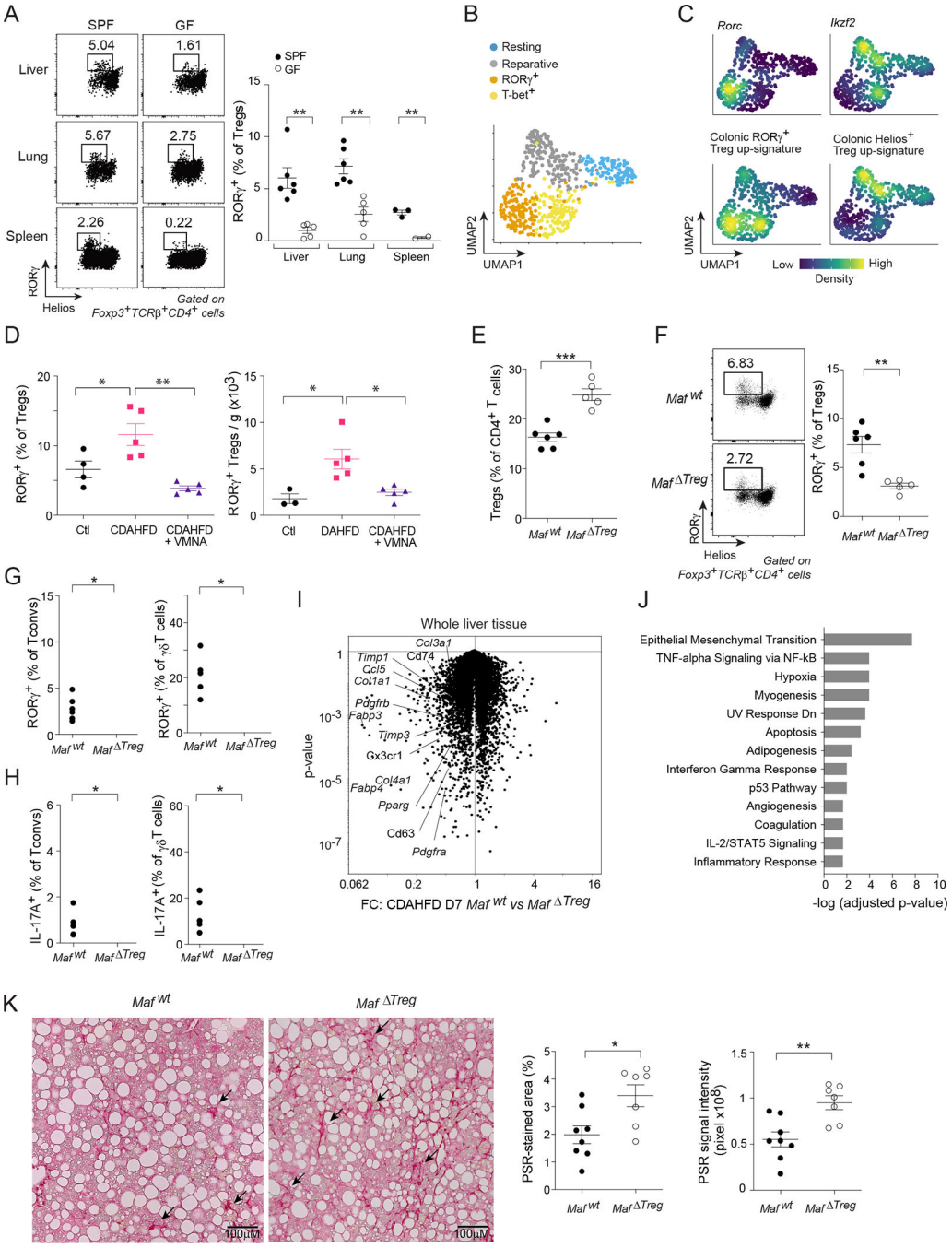

Figure 7: Generality of RORγ$^+$ Treg cells' role in regulating tissue inflammation

(A) RORγ$^+$ Treg cell fractions in diverse tissues of SPF and GF mice. (B, C) scRNA-seq of cardiac muscle Treg cells after myocardial infarction[57]. B) 2D UMAP plot. C) Density plot of the indicated genes and signatures. (D) Quantification of liver RORγ$^+$ Treg cells after one week of feeding with control diet (Ctl) or choline-deficient, L-amino acid-defined, high-fat diet (CDAHFD) ± VMNA treatment. (E-J) *Maf*$^{\Delta Treg}$ or *Maf*^{wt} mice were fed with CDAHFD for one week. Quantification of liver E) total Treg cells; F) RORγ$^+$ Treg cells; G) RORγ$^+$ Tconv (left) and γδT cells (right); and H) IL-17A expression. I) Volcano plot illustrating

the transcriptional differences in livers from the two genotypes. J) Pathway analysis of transcripts significantly up-regulated ≥ 1.5-fold in $Maf^{\Delta Treg}$ livers. (K) Mice were fed with CDAHFD for 8 weeks. Representative images (left) and summary data (right) of liver PSR staining. Representative dot-plots and images are from 2 independent experiments. Unpaired t-test (A, D-F, K), or paired t-test (G, H). See also Figure S7.

KEY RESOURCES TABLE

REAGENT or RESOURCE	SOURCE	IDENTIFIER
Antibodies		
Brilliant Violet 605™ anti-mouse CD45 (clone 30-F11)	Biolegend	Cat# 103140
APC anti-mouse CD45 (clone 30-F11)	Biolegend	Cat# 103112
PE anti-Mouse TCRβ (clone H57-597)	Biolegend	Cat# 109208
BUV737 anti-Mouse TCRβ (clone H57-597)	BD	Cat# 612821
Brilliant Violet 711™ anti-mouse CD4 (Clone RM4-5)	Biolegend	Cat# 100550
PE-eFluor™ 610 anti-mouse CD4 (clone RM4-5)	eBioscience	Cat# 61-0042-82
APC/Cyanine7 anti-mouse CD8a (clone 53-6.7)	Biolegend	Cat# 100714
Brilliant Violet 605™ anti-mouse CD45 (clone 30-F11)	Biolegend	Cat# 103140
PerCP/Cyanine5.5 anti-mouse CD45.1 (clone A20)	Biolegend	Cat# 110728
APC/Cyanine7 anti-mouse CD45.2 (clone 104)	Biolegend	Cat# 109824
PE/Cyanine7 anti-mouse CD90.1 (clone OX-7)	Biolegend	Cat# 202518
PerCP/Cyanine5.5 anti-mouse CD44 (clone IM7)	Biolegend	Cat# 103032
APC anti-mouse CXCR6 (clone SA051D1)	Biolegend	Cat# 151106
Brilliant Violet 711™ anti-mouse CD25 (clone PC61)	Biolegend	Cat# 102049
PerCP/Cyanine5.5 anti-mouse CD11b (clone M1/70)	Biolegend	Cat# 101228
APC/Cyanine7 anti-mouse Ly6G (Clone 1A8)	Biolegend	Cat# 127624
APC/Cyanine7 anti-mouse CD3ε (clone 145-2C11)	Biolegend	Cat# 100330
PE/Cyanine7 anti-mouse TCRγδ (clome GL3)	Biolegend	Cat# 118124
Pacific Blue™ anti-mouse CD31 (clone 390)	Biolegend	Cat# 102422
FITC anti-mouse Ly-6A/E (Sca-1; clone E13-161.7)	Biolegend	Cat# 122505
PE/Cyanine7 anti-mouse VCAM-1 (clone 429)	Biolegend	Cat# 105720
PE-Cyanine7 anti-ST2 (clone RMST2-2)	eBioscience	Cat# 25-9335-82
Pacific Blue™ anti-mouse Helios (clone 22F6)	Biolegend	Cat# 137220
Brilliant Violet 785™ anti-T-bet (clone 4B10)	Biolegend	Cat# 644835
APC anti-Foxp3 (clone FJK-16s)	eBioscience	Cat# 17-5773-82
Alexa Fluor™ 488 anti-Foxp3 (clone FJK-16s)	eBioscience	Cat# 53-5773-82
PE anti-RORγt (clone AFKJS-9)	eBioscience	Cat# 12-6988-82
APC anti-RORγt (clone AFKJS-9)	eBioscience	Cat# 17-6988-82
PE-Cyanine7 anti-c-Maf (clone sym0F1)	eBioscience	Cat# 25-9855-82
Alexa Fluor™ 488 anti-Gata3 (clone TWAJ)	eBioscience	Cat# 53-9966-42
Alexa Fluor® 488 anti-mouse IL-17A (clone TC11-18H10.1)	Biolegend	Cat# 506910
Brilliant Violet 785™ anti-mouse IFN-γ (clone XMG1.2)	Biolegend	Cat# 505838
PE anti-mouse IL-4 (clone 11B11)	Biolegend	Cat# 504104
PE anti-mouse IL-5 (clone TRFK5)	Biolegend	Cat# 504304
PE anti-IL-13 (clone eBio13A)	eBioscience	Cat# 12-7133-81
Alexa Fluor® 700 anti-Ki-67 (clone B56)	BD	Cat# 561277

REAGENT or RESOURCE	SOURCE	IDENTIFIER
Biotin anti-Areg (polyclonal)	R&D	Cat# BAF989
Alexa Fluor® 647 anti-cleaved Caspase-3 (Asp175; clone D3E9)	Cell Signaling	Cat# 9602S
TotalSeq-A anti-mouse hashtags	Biolegend	Cat# 155811 Cat# 155813 Cat# 155815 Cat# 155817 Cat# 155819 Cat# 155821 Cat# 155823
TotalSeq-C anti-mouse hashtags	Biolegend	Cat# 155861 Cat# 155863 Cat# 155865 Cat# 155867 Cat# 155869 Cat# 155871 Cat# 155873 Cat# 155875 Cat# 155877
Anti-Myogenin (clone F5D)	Santa Cruz	Cat# sc-12732
Anti-Myosin Heavy Chain (clone MF20)	R&D	Cat# MAB4470
Cy™3 Donkey Anti-Mouse IgG	Jackson ImmunoResearch	Cat# 715-165-150
*In Vivo*MAb anti-mouse/human/rat CCL2 (clone 2H5)	BioXCell	Cat# BE0185
In VivoMAb polyclonal Armenian hamster IgG	BioXCell	Cat# BE0091
*In Vivo*MAb anti-mouse MHC Class II (I-A/I-E) (clone M5/114)	BioXCell	Cat# BE0108
In VivoMAb rat IgG2b control (clone LTF-2)	BioXCell	Cat# BE0090
Bacterial and Virus Strains		
Clostridium ramosum	Geva-Zatorsky et al.,2017[96]	NA
Peptostreptococcus magnus	Geva-Zatorsky et al.,2017[96]	NA
Chemicals, peptides, and recombinant proteins		
Cardiotoxin from *Naja mossambica*	Sigma-Aldrich	Cat# C9759
Cardiotoxin from *Naja pallida*	Sigma-Aldrich	Cat# 217503
FTY720	Cayman Chemical	Cat# 10006292
CP-105696	Sigma-Aldrich	Cat# PZ0363
Diphtheria Toxin	Sigma-Aldrich	Cat# D0564
Recombinant murine IL-17A	Peprotech	Cat# 210-17
Metronidazole	Sigma-Aldrich	Cat# M1547
Ampicillin	Sigma-Aldrich	Cat# A0166
Neomycin	Fisher Scientific	Cat# BP2669-25
Vancomycin	RPI	Cat# 1404-93-9
FITC-Dextran, 4 kDa	Chondrex	Cat# 4013
Collagenase type II (Gibco)	Thermo Fisher Scientific	Cat# 17101015
Collagenase type IV (Gibco)	Thermo Fisher Scientific	Cat# 17104-019
Dispase	Thermo Fisher scientific	Cat# 17105041
DNase I from bovine pancreas	Sigma-Aldrich	Cat# DN25
Phorbol 12-Myristate 13-acetate (PMA)	Sigma-Aldrich	Cat# P8139
Ionomycin	Sigma-Aldrich	Cat# I0634

REAGENT or RESOURCE	SOURCE	IDENTIFIER
Protein Transport Inhibitor Cocktail	eBioscience	Cat# 00-4980-03
Percoll	GE Healthcare	Cat# 17089109
2-Mercaptoethanol	Sigma-Aldrich	Cat# M7522
TCL RNA lysis buffer	Qiagen	Cat# 1031576
TRIzol	Invitrogen	Cat# 15596026
Critical commercial assays		
Foxp3 / Transcription Factor Staining Buffer Set	eBioscience	Cat# 00-5523-00
Click-iT™ EdU Cell Proliferation Kit for Imaging, Alexa Fluor™ 488 dye	Thermo Fisher Scientific	Cat# C10337
Zombie UV™ Fixable Viability Kit	Biolegend	Cat# 423108
RNeasy Lipid Tissue Mini Kit	Qiagen	Cat# 74804
RNAClean XP beads	Beckman Coulter	Cat# A63987
Nextera DNA Sample Prep Kit	Illumina	Cat# FC-121-1030
Chromium Single Cell 3’ GEM, Library & Gel Bead Kit v3	10x	Cat# PN-1000092
Chromium Single Cell B Chip Kit	10x	Cat# PN-1000074
Chromium i7 Multiplex Kit	10x	Cat# PN-120262
Chromium Next GEM Single Cell 5’ Library & Gel Bead Kit v1.1	10x	Cat# PN-1000167
Chromium Single Cell 5’ Library Construction Kit	10x	Cat# PN-1000020
Chromium Single Cell 5’ Feature Barcode Library Kit	10x	Cat# PN-1000080
Chromium Single Cell V(D)J Enrichment Kit, Mouse T Cell	10x	Cat# PN-1000071
Chromium Next GEM Chip G Single Cell Kit	10x	Cat# PN-1000127
Single Index Kit T Set A	10x	Cat# PN-1000213
Single Index Kit N Set A	10x	Cat# PN-1000212
123count eBeads	Invitrogen	Cat# 01-1234-42
Deposited data		
scRNA-seq/sc *Tcr*-seq of muscle and colon Treg cells	This paper	GSE196337
Bulk RNA-seq	This paper	GSE195966
scRNA-seq of colon CD4$^+$ T cells	Kiner et al., 2021[88]	GSE160053
scRNA-seq of muscle Treg cells at day 4 after injury	DiSpirito et al., 2018[28]	GSE109742
scRNA-seq of whole muscle	Oprescu et al., 2020[50]	GSE138826
scRNA-seq of injured heart CD4$^+$ T cells	Xia et al., 2020[57]	GSE155619
Experimental models: Organisms/strains		
Mouse: C57BL/6J	Jackson Laboratory	000664
Mouse: B6.CD45.1	Jackson Laboratory	002014
Mouse: B6.129P2-*Tcrb*^{tm1Mom}/J	Jackson Laboratory	002118
Mouse: B6.129P2(Cg)-*Rorc*$^{tm2Litt/J}$	Jackson Laboratory	007572
Mouse: B6.*Foxp3*^{GFP}	Bettelli et al., 2006[79]	N/A
Mouse: B6.*Foxp3*$^{Thy1.1}$	Liston et al., 2008[81]	N/A
Mouse: B6.*Foxp3*^{DTR}	Kim, et al., 2007[82]	N/A
Mouse: B6.Kaede	Tomura et al., 2008[30]	N/A

REAGENT or RESOURCE	SOURCE	IDENTIFIER
Mouse: B6.*Foxp3*^{Cre}	Rubtsov et al., 2008[83]	N/A
Mouse: B6.*Maf*$^{fl/fl}$	Wende et al, 2012[84]	N/A
Germ Free C57BL/6J mice	GF C57BL/6 colony housed in the animal facility at Harvard Medical School.	N/A
Software and algorithms		
Cell Ranger (v2.1.0, v4.0.0 and v6.0.0)	10X Genomics	
CITE-seq-count v1.4.3	doi:10.5281/zenodo.2590196	https://hoohm.github.io/CITE-seq-Count/
R v4.1.1	The R Foundation	https://www.r-project.org
Seurat v4.0.3	Hao et al., 2021[97]	https://satijalab.org/seurat/
Harmony v0.1.0	Korsunsky et al., 2019[92]	
Nebulosa v1.3.0	Alquicira-Hernandez et al., 2021 [91]	https://www.bioconductor.org/packages/release/bioc/html/Nebulosa.html
scRepertoire v1.4.0	Borcherding et al., 2020 [32]	https://github.com/ncborcherding/scRepertoire
Cuffquant version 2.2.1	Trapnell et al., 2012[98]	http://cole-trapnell-lab.github.io/cufflinks/install/
DESeq2 v1.28.1	Love et al, 2014[99]	https://bioconductor.org/packages/release/bioc/html/DESeq2.html
Limma	Ritchie et al, 2015 [100]	https://bioconductor.org/packages/release/bioc/html/limma.html
GenePattern software package	Broad Institute	http://software.broadinstitute.org/cancer/software/genepattern/
maSigPro	Nueda et al., 2014[93]	https://www.bioconductor.org/packages/release/bioc/html/maSigPro.html
Scanpy	Wolf et al., 2018[101]	https://github.com/scverse/scanpy
Metascape	Zhou et al., 2019 [102]	https://metascape.org/

REAGENT or RESOURCE	SOURCE	IDENTIFIER
Enrichr	Kuleshov et al., 2016[103]	https://maayanlab.cloud/Enrichr/
PRISM v9.2.0	GraphPad	https://www.graphpad.com
FlowJo 10.6.2	FlowJo, LLC	https://www.flowjo.com
ImageJ v2.1.0/1.53c	Schindelin et al., 2012[95]	https://imagej.net/software/fiji/
Other		
Control diet: L-Amino Acid Rodent Diet With 10 kcal% Fat (Amino Acid Complete)	Research Diets	Cat# A08051501i
CDAHFD: L-Amino Acid Diet With 45 kcal% Fat With 0.1% Methionine and No Added Choline	Research Diets	Cat#: A06071309i